JGR Solid Earth

RESEARCH ARTICLE

Key Points:
- We present a rock magnetic record of high sedimentation events in Bay of Bengal
- We investigate the controls of rapid sedimentation and shale-tectonism on the development of the fracture-filled gas hydrate system in the Krishna-Godavari (K-G) basin
- We have developed a magnetic proxy to constrain paleo-CH_4 seepage events in marine sediments

Supporting Information:
- Supporting Information S1
- Data Set S1

Correspondence to:
F. Badesab,
firoz@nio.org

Magnetic Mineralogical Approach for the Exploration of Gas Hydrates in the Bay of Bengal

Firoz Badesab[1] iD, Pawan Dewangan[1] iD, Virsen Gaikwad[1], Myriam Kars[2] iD, Muralidhar Kocherla[1] iD, Kolluru S. Krishna[3], Satish J. Sangode[4], Kannan Deenadayalan[5] iD, Pushpendra Kumar[6], Omkar Naikgaonkar[1], Mohammad Ismaiel[3] iD, and Aarbaz Khan[1]

[1]National Institute of Oceanography, CSIR, Dona Paula, Goa, India, [2]Centre for Advanced Marine Core Research, Kochi University, Nankoku, Japan, [3]Centre for Earth, Ocean and Atmospheric Sciences, University of Hyderabad, Hyderabad, India, [4]Department of Geology, Savitribai Phule Pune University, Pune, India, [5]Indian Institute of Geomagnetism, New Panvel, Navi Mumbai, India, [6]Oil and Natural Gas Corporation Ltd., Institute of Engineering and Ocean Technology, Panvel, Navi Mumbai, India

Abstract We evaluate the environmental magnetic, geochemical, and sedimentological records from three sediment cores from potential methane-hydrate bearing sites to unravel linkages between sedimentation, shale tectonics, magnetite enrichment, diagenesis, and gas hydrate formation in the Krishna-Godavari basin. Based on downcore rock magnetic variations, four sedimentary magnetic property zones (I–IV) are demarcated. A uniform band of enhanced magnetic susceptibility (zone III) appears to reflect a period of high-sedimentation events in the Krishna-Godavari basin. Highly pressurized sedimentary strata developed as a result of increased sedimentation that triggered the development of a fault system that provided conduits for upward methane migration to enter the gas hydrate stability zone, leading to the formation of gas hydrate deposits that potentially seal the fault system. Magnetic susceptibility fluctuations and the presence of iron sulfides in a magnetically enhanced zone suggest that fault system growth facilitated episodic methane venting from deeper sources that led to multiple methane seepage events. Pyrite formation along sediment fractures resulted in diagenetic depletion of magnetic signals and potentially indicates paleo sulfate-methane transition zone positions. We demonstrate that a close correlation between magnetic susceptibility and chromium reducible sulfur concentration can be used as a proxy to constrain paleomethane seepage events. Our findings suggest that the interplay between higher sedimentation events and shale tectonism facilitated fluid/gas migration and trapping and the development of the gas hydrate system in the Krishna-Godavari basin. The proposed magnetic mineralogical approach has wider scope to constrain the understanding of gas hydrate systems in marine sediments.

1. Introduction

Gas Hydrates are distributed widely in oceanic and permafrost regions and store immense quantities of methane gas (Kvenvolden, 1993). In the last few decades, there has been emphasis on understanding natural gas hydrate reservoirs as potential alternative energy resources (Boswell & Collett, 2011; Kvenvolden, 1988), for estimating global carbon budgets (Dickens et al., 1995), and for understanding the role of methane as a greenhouse gas and a significant contributor to climate change (Archer & Buffett, 2005; Kennett et al., 2000). Geodynamics, tectonism, global climatic change, sea level fluctuations, and variable sedimentation rate can affect the development of gas hydrate systems in marine sedimentary environments (García-Tortosa et al., 2011; Herbozo et al., 2013; Milkov & Sassen, 2002; Moore et al., 2015; Paull et al., 1991). For example, neo-tectonic activity can potentially alter the base of the gas hydrate stability zone, leading to the gas hydrate dissociation and intensified methane expulsion/seepage events (Dewangan et al., 2008; Goto et al., 2016; Jahren et al., 2005; Riedel et al., 2011; von Huene & Pecher, 1999). Rapid sediment loading triggered by abrupt climatic changes and supply from major river systems can generate overpressured sedimentary strata, thereby creating an efficient fluid migration system and sedimentary reservoir for methane trapping and gas hydrate formation (Hustoft et al., 2009; Karstens et al., 2018; Torres et al., 2008; Wang et al., 2011; Yu et al., 2014).

Magnetic iron minerals are widespread and indicative of sedimentary constituents, and their associated magnetic signals can reflect primary depositional and secondary diagenetic processes (Canfield, 1989). Sediment provenance, sedimentation rate, transportation, and depositional conditions determine the concentration, grain size, and mineralogy of magnetic minerals and can significantly affect sediment

magnetic records (Thompson & Oldfield, 1986; Verosub & Roberts, 1995). Diagenetic processes can also lead to primary magnetic mineral dissolution and precipitation of secondary magnetic minerals (Roberts, 2015). Soon after deposition, primary iron mineral assemblages pass through a sequence of early diagenetic processes in which the minerals undergo alteration. One major pathway is the reaction with hydrogen sulfide via sulfate reduction coupled with anaerobic oxidation of methane (AOM), which is driven by bacterial organic matter decomposition (Berner, 1970; Canfield, 1989; Ferdelman et al., 1999; Froelich et al., 1979; Jørgensen, 1982). Diagenetic reactions involved in iron (oxyhydr)oxide reduction by hydrogen sulfide and subsequent iron sulfide formation is well described by Karlin and Levi (1983) and Channell and Hawthorne (1990).

In gas hydrate environments, AOM is an important biogeochemical process that results from the interaction of upward methane flux and downward sulfate flux (Knittel & Boetius, 2009; Treude et al., 2005). Sulfate reduction coupled with AOM generates huge amounts of hydrogen sulfide into pore waters, which reacts further with dissolved iron to form magnetic iron sulfides, thereby creating distinct secondary magnetic signals in the AOM zone (Berner, 1970; Canfield & Berner, 1987; Dewangan et al., 2013; Jørgensen et al., 2004; Leslie et al., 1990; Riedinger et al., 2005; van Dongen et al., 2007). Changes in any of sedimentation rate, supply of organic matter, sulfate, reactive iron, and methane can significantly affect hydrogen sulfide generation that in turn influences the diagenetic alteration of magnetic minerals (Borowski et al., 1996; Dewangan et al., 2013; Kasten et al., 1998, 2003; Riedinger et al., 2005; Roberts, 2015). Rock magnetic investigation has the potential to distinguish between primary magnetic signals from detrital minerals and secondary signals that occur due to diagenetic alteration of primary magnetic minerals in gas hydrate depositional environments. Therefore, rock magnetic techniques can provide important information on different forcing factors (climate, tectonics, and sedimentation) that affect gas hydrate formation in marine sediments.

Rock magnetic studies of gas hydrate environments have focused primarily on understanding diagenetic alteration of detrital magnetic minerals (Dewangan et al., 2013; Enkin et al., 2007; Esteban et al., 2008; Johnson & Phillips, 2014; Riedinger et al., 2005; Shi et al., 2017), exploring linkages between magnetic iron sulfides and gas hydrates (Housen & Musgrave, 1996; Kars & Kodama, 2015a, 2015ab; Larrasoaña et al., 2007; Musgrave et al., 2006), deciphering controls on gas hydrate system evolution (Badesab et al., 2017), rock magnetic properties of gas hydrate bearing sediments (Kars & Kodama, 2015a, 2015ab), and developing proxies for tracking paleomethane seepage events (Novosel et al., 2005; Panieri et al., 2016; Usapkar et al., 2014) and paleo sulfate-methane transition zone (SMTZ) boundaries (Johnson et al., 2014; Peketi et al., 2012). However, detailed rock magnetic studies that focus on unravelling linkages between sedimentation, shale-tectonism, sediment diagenesis, and gas hydrate formation in marine sedimentary systems are still lacking.

A recent rock magnetic study conducted (Badesab et al., 2017) on a sediment core (NGHP-01-10D) overlying methane hydrate deposits from the Krishna-Godavari (K-G) basin examined the sediment magnetic signature of detrital and diagenetic processes associated with the evolution of a fracture-filled gas hydrate system. An anomalous magnetic susceptibility zone within gas hydrate bearing intervals at site NGHP-01-10D was reported. However, linkages between magnetic enhancement and gas hydrate formation were poorly resolved. Sediment cores collected during the first Indian National Gas Hydrate Drilling Expedition (NGHP-Exp-01) record the history of sedimentation, shale tectonics, and geochemical processes that influenced gas hydrate system development in the K-G basin (Kumar et al., 2014) and offer an excellent opportunity to obtain a long-term view of magnetic mineral diagenesis in marine gas hydrate sediments. In the present study, we carried out comprehensive rock magnetic measurements complemented by sedimentological analyses of three long sediment cores NGHP-01-03B (299.5 m), NGHP-01-05C (194.9 m), and NGHP-01-07B (199.08 m), which provides the longest and most detailed sediment magnetic record available so far from the K-G basin. Our work focuses on fingerprinting complex magnetic mineralogical signatures associated with gas hydrate related processes, and we present a method for magnetic exploration of gas hydrates in marine sedimentary systems.

2. Materials and Methods

The study area lies on the continental slope of K-G basin (Figure 1), which is a proven petroliferous basin of India (Bastia, 2007). The K-G basin is a pericratonic rift basin situated in the central eastern continental
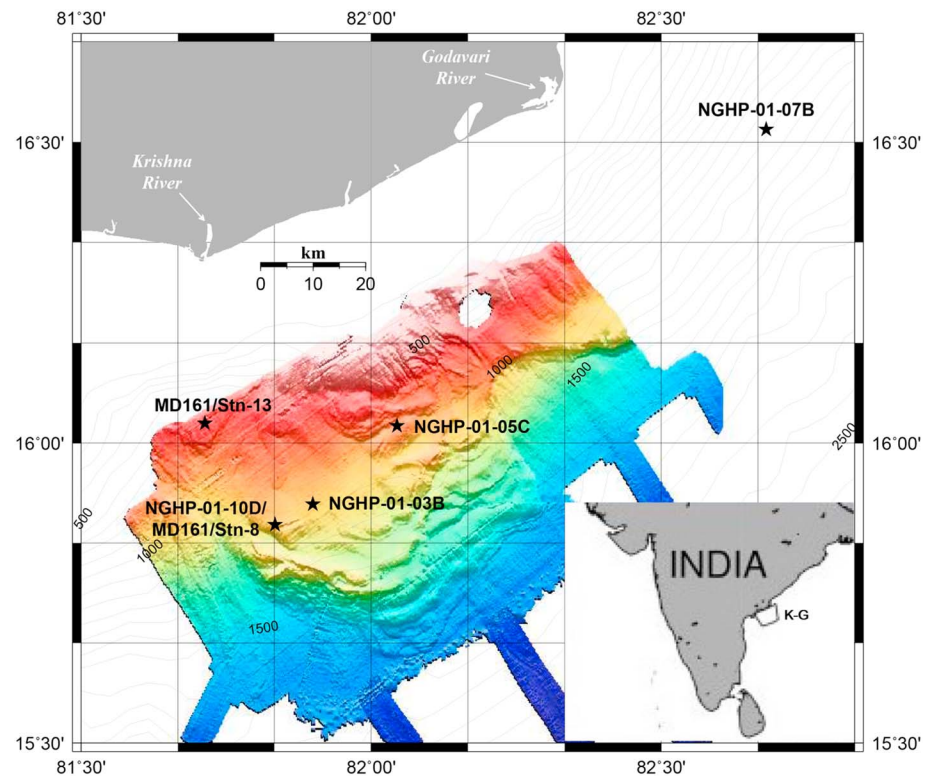
Figure 1. Location map of sediment cores NGHP-01-10D, NGHP-01-03B, NGHP-01-05C, NGHP-01-07B, MD161/Stn-8, and MD161/Stn-13 in the Krishna-Godavari basin, Bay of Bengal.

margin of India. Sediment thicknesses of 3–5 km in the onshore region and about 8 km in the offshore region have been reported (Bastia, 2007; Prabhakar & Zutshi, 1993). The Krishna and Godavari river systems deliver most of the sediment to this basin. Holocene-Pleistocene sedimentary deposits in the K-G basin are dominated by smectite-bearing Godavari clay formations (Rao, 2001). The estimated annual sediment transport of the Krishna and Godavari rivers is around 67.7 and 170×10^6 t, respectively (Biksham & Subramanian, 1988; Ramesh & Subramanian, 1988). The presence of subsurface gas hydrate deposits in the K-G basin has been confirmed through drilling and sediment coring (Collett et al., 2008). Neotectonic activity in the K-G basin led to the formation of different types of geomorphic structures on the sea floor, including shale diapirs, faults, and mounds. The fault systems associated with bathymetric mounds facilitate fluid/gas migration and provide favorable sedimentary structures for gas hydrate reservoir formation in the K-G basin (Dewangan et al., 2010). The studied core NGHP-01-05C is located on a mound, and core NGHP-01-03B is from the slope basin. Core NGHP-01-07B is from close to a submarine channel near Godavari delta.

2.1. Sampling and Measurements

The studied sediment cores (NGHP-01-03B, NGHP-01-05C, and NGHP-01-07B) were subsampled at 1.5- to 6-m intervals. For magnetic analysis, 135 subsamples were dried, weighed, and packed in 25-mm cylindrical sample bottles. Measurements were carried out at the paleomagnetic laboratory of CSIR-National Institute of Oceanography (CSIR-NIO), Goa, India.

2.2. Rock Magnetic Analysis

Low-field magnetic susceptibility measurements were carried out using a Bartington Instruments MS2B dual frequency susceptibility meter. The susceptibility was measured at two (low and high) frequencies $\chi_{lf} = 0.47$ kHz and $\chi_{hf} = 4.7$ kHz. The frequency-dependent susceptibility was calculated as $\chi_{fd}\% = (\chi_{lf} - \chi_{hf})/\chi_{lf} \times 100\%$. An anhysteretic remanent magnetization (ARM) was imparted using a 100-mT alternating field with a superimposed fixed direct current (DC) bias field of 50 μT and was measured using a Molspin Minispin spinner magnetometer. Susceptibility of ARM (χ_{ARM}) is calculated as the mass-normalized ARM divided by the DC bias field. An isothermal remanent magnetization (IRM) was

imparted in an inducing field of +1 T in the forward direction and was demagnetized by DC backfields at −20, −30, −100, and −300 mT using a MMPM10 pulse magnetizer. The respective remanences were measured using a Molspin Minispin magnetometer. The mass-normalized IRM acquired at a peak field of 1 T is considered to be the saturation IRM (SIRM). S ratio is calculated as the ratio between the IRM at −300 mT and SIRM ($IRM_{-300mT}/SIRM_{1T}$; Thompson & Oldfield, 1986). Temperature-dependent magnetic susceptibility (χ-T) measurements on 15 selected samples were carried out at the Indian Institute of Geomagnetism in a 300-A/m field at 875 Hz with a CS-3 furnace coupled to an Agico (KLY-4S) Kappabridge system. High-temperature measurements were performed from room temperature to 700 °C in an argon atmosphere. Hysteresis loops, first-order reversal curves (FORC; Pike et al., 1999), and back-field demagnetization curves were also measured for 22 selected samples with a saturating field of 1 T (field increment of 4 mT, averaging time of 200 ms, and a slew rate limit of 1 T/s) at the Center for Advanced Marine Core Research, Kochi University, Japan. FORC diagrams were processed using the FORCinel software (Harrison & Feinberg, 2008).

Low-temperature magnetic measurements were performed at the Center for Advanced Marine Core Research. A Quantum Design Magnetic Properties Measurement System was used for remanence measurements on representative samples covering the four sediment zones of cores NGHP-01-05C and NGHP-01-07B. A RT-SIRM was imparted at room temperature (300 K) in 2.5 T. Samples were then cooled to 5 K and warmed back to 300 K in a zero magnetic field. A LT-SIRM was then imparted at 5 K in 2.5 T. Samples were warmed up to 300 K in a zero magnetic field (termed "ZFC" for zero field-cooled). Samples were then cooled to 5 K in the presence of a 2.5 T magnetic field. A LT-SIRM was again imparted at 5 K, and samples were warmed to 300 K in a zero magnetic field (termed "FC" for field-cooled). Magnetic parameters were normalized by sample mass. δ_{FC} and δ_{ZFC} were calculated following Moskowitz et al. (1993) to differentiate the origin of magnetite (biogenic or inorganic). δ is a measure of the amount of remanence lost during warming through the Verwey transition.

2.3. Sedimentological Analyses
2.3.1. Grain Size Measurements
Sediment grain size measurements were carried out using a Malvern Mastersizer 2000 Laser Particle Size Analyzer at CSIR-NIO. Sediment samples were first desalinated and were later decarbonated using dilute HCl (1 N). Sediment suspensions were treated with 10% H_2O_2 to remove organic carbon, and the dispersing agent Na-hexametaphosphate was added to the suspension, which was then ultrasonicated prior to analysis. Grain size values are presented as volume %.
2.3.2. Mineralogical Analysis
Magnetic particles were separated from the bulk sediment following the extraction method of Petersen et al. (1986). Images of magnetic particles were captured in secondary electron imaging mode at energy levels between 15 and 20 keV using a scanning electron microscope (SEM; JEOL JSM-5800 LV). The composition of magnetic particles was determined using an energy dispersive X-ray spectroscopy (EDS) probe attached to the microscope. The magnetic mineralogy of representative samples from all three sediment cores was determined using a Rigaku X-Ray Diffractometer (Ultima IV). The samples were run from 15° to 70° of 2θ at 1°/min scan speed using Cu Kα radiation (λ = 1.5414 Å).

2.4. Geochemical Analyses
Chromium reducible sulfur (CRS) contents of the studied sediment cores (MD161/Stn8, MD161/Stn13, and NGHP-01-10D) were made following Peketi et al. (2012, 2015). Pore water sulfate and methane data for the sediment cores (NGHP-01-10D, NGHP-01-03B, NGHP-01-05C, and NGHP-01-07B) are presented in Figure S3 in the supporting information. These data are from Collett et al. (2008).

2.5. Geophysical Data
High-resolution seismic data for sites NGHP-01-10D, NGHP-01-03B, and NGHP-01-05C are from Ramprasad et al. (2011) and Anitha et al. (2014). An interpreted seismic section is shown in Figure S2.

3. Results

3.1. Downcore Rock Magnetic Property Variations

Based on downcore magnetic property changes in sediment cores NGHP-01-03B, NGHP-01-05C, and NGHP-01-07B, four sediment zones (Z-I, Z-II, Z-III, and Z-IV) are identified (Figures 3a–3o). A largely uniform and extended thickness of enhanced magnetic susceptibility is present in all four sediment cores (Figures 2a–2d). The topmost zone (Z-I) of cores NGHP-01-03B, NGHP-01-05C, and NGHP-01-07B contains a decreasing χ_{lf} and SIRM trend, which suggests a downcore reduction in magnetic mineral concentration (Figures 3a, 3b, 3f, 3g, 3k, and 3l). The lower ARM/SIRM and higher S ratio (0.90–1.0) in NGHP-01-03B and NGHP-01-05C reflect the dominance of coarse-grained magnetite in this zone (Figures 3c, 3d, 3h, and 3i), while higher ARM/SIRM in NGHP-01-07B indicates the presence of fine-grained magnetic particles (Figure 3m). A noticeable decrease in concentration of magnetic minerals is observed in Z-II as reflected by low χ_{lf} and SIRM values (Figures 2a, 2b, 2c, 2d, 3f, 3g, 3k, and 3l). Z-III is marked by a sudden increase in magnetic mineral concentration as reflected in χ_{lf} and SIRM (Figures 3a, 3b, 3f, 3g, 3k, and 3l). Higher S ratios suggest the predominance of ferrimagnetic minerals in this zone (Figures 3d, 3i, and 3n). A substantial drop in χ_{lf} and SIRM coincides with the depth of the BSR in core NGHP-01-05C (Figures 3f–3g). A similar drop in χ_{lf}, SIRM, and S ratio is observed below the present-day BSR in NGHP-01-03B and well above in NGHP-01-07B (Figures 3a, 3b, 3d, 3k, 3l, and 3n). Within Z-III, a few minor χ_{lf} drops are also evident (Figures 3a, 3f, and 3k). A minor increase in χ_{lf} and SIRM occurs in Z-IV of NGHP-01-05C and NGHP-01-07B, while an opposite trend is observed in NGHP-01-03B (Figures 3a, 3b, 3f, 3g, 3k, and 3l). A pronounced ARM/SIRM increase in Z-IV of NGHP-01-03B reflects a finer magnetic mineral grain size (Figure 3c). A notable sediment grain size increase is seen in Z-III of cores NGHP-01-05C and NGHP-01-07B, while no distinct trend occurs in core NGHP-01-03B (Figures 3e, 3j, and 3o).

3.2. Magnetic Mineralogical and Granulometric Proxies

3.2.1. Temperature-Dependent Magnetic Susceptibility

χ-T curves of representative samples from Z-I, Z-II, Z-III, and Z-IV of cores NGHP-01-03B, NGHP-01-05C, and NGHP-01-07B are shown in Figure 4. A sharp magnetic susceptibility decrease between 570 and 600 °C suggests that the bulk magnetic mineralogy is dominated by magnetite (Dunlop et al., 1997; Figures 4a–4l). The χ increase between 300 and 500 °C is likely due to conversion of paramagnetic minerals such as pyrite and iron-bearing silicates, iron-rich carbonates, siderite, and iron-rich smectites into magnetite during heating (Cui et al., 2017; Hirt et al., 1993; Hirt & Gehring, 1991; Pan et al., 2000; Passier et al., 2001; Philips, 2018; Figures 4a–4l).

3.2.2. Low-Temperature Magnetometry

Low-temperature measurements for representative samples from different magnetic zones of cores NGHP-01-05C and NGHP-01-07B are characteristic of the different magnetic minerals present in the studied samples (Figure 5). For samples from Z-I, a Verwey transition due to detrital magnetite (T_v 118–120 K) is evident in RT-SIRM, in the first derivative of magnetization curves, and the remanence did not recover fully during warming (Figures 5a–5d; Chang, Heslop, et al., 2016; Muxworthy & McClelland, 2000; Özdemir et al., 2002; Verwey, 1939). Samples from the magnetically reduced zone (Z-II) of core NGHP-01-05C do not provide evidence of a Verwey transition in RT-SIRM, ZFC-FC, and the first derivative of magnetization curves (Figures 5e–5f). Nearly 60% of the LT-SIRM imparted at 5 K is lost during warming between 5 and 35 K (Figures 5e–5f). This indicates the presence of superparamagnetic (SP) magnetic particles (Passier & Dekkers, 2002; Tarduno et al., 1995). It is highly likely that the SP magnetic particles are greigite because fine magnetite particles would dissolve in sulfidic settings, while the SP greigite nanoparticles would be thermodynamically more stable in contrast to SP magnetite nanoparticles (Roberts et al., 2018; Rowan et al., 2009). Samples from the same zone (Z-II) of core NGHP-01-07B have a Verwey transition at ~120 K in the RT-SIRM and the first derivative of magnetization curves, which indicates the presence of detrital magnetite (Chang, Heslop, et al., 2016; Figures 5g and 5h). Samples from the magnetically enhanced zone (Z-III) of core NGHP-01-07B have a well-developed Verwey transition in RT-SIRM and the first derivative of magnetization curves (Figures 5k and 5l). The remanence does not recover totally during warming of RT-SIRM. In the same zone (Z-III) of NGHP-01-05C, the Besnus transition at ~35 K is typical of detrital pyrrhotite as evident in the RT-SIRM cooling and the first derivative of magnetization curves (Dekkers, 1989; Horng & Roberts, 2006; Rochette et al., 1990; Figures 5i and 5j), but lack of such a transition is not diagnostic of authigenic
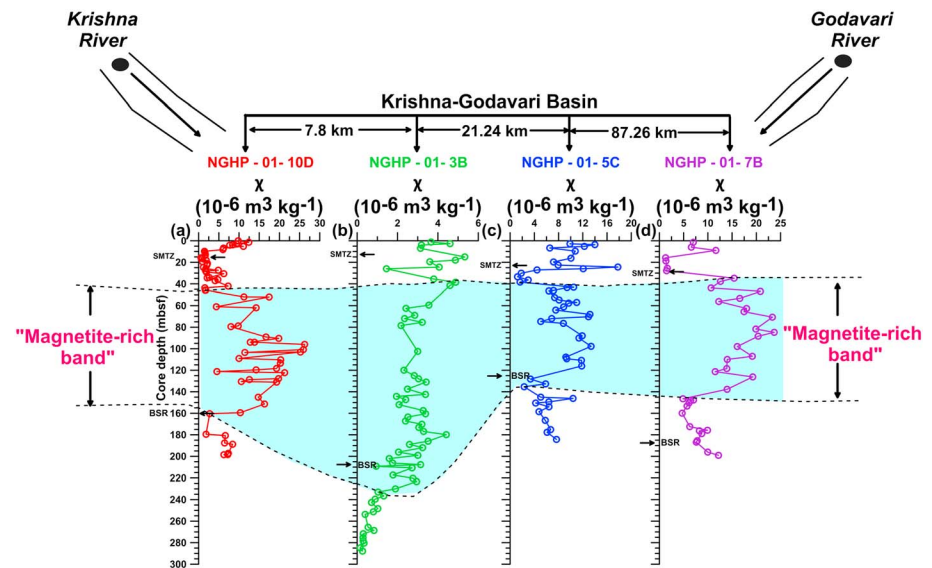
Figure 2. (a–d) Downcore variations of magnetic susceptibility (χ) in sediment cores (NGHP-01-10D, NGHP-01-03B, NGHP-01-05C, and NGHP-01-07B) from the K-G basin. Increased magnetic susceptibility in zone-III is highlighted by a blue band. The distance between the core locations, depth of the bottom simulating reflector (BSR) and the position of the sulfate-methane transition zone (SMTZ) are also marked. Magnetic susceptibility data for core NGHP-01-10D are from Badesab et al. (2017).

pyrrhotite, which lacks a low-temperature transition (Horng & Roberts, 2018). The remanence recovers totally during warming of the RT-SIRM, which suggests the occurrence of a single domain pyrrhotite. We did not observe any typical pyrrhotite features in the ZFC-FC curves. Higher T_v value in the samples from Z-I and Z-III are indicative of detrital magnetite (Chang, Heslop, et al., 2016; Figures 5b, 5d, 5j, and 5l). Below the present-day BSR, that is, Z-IV, magnetic characteristics are similar to those of Z-II (Figures 5e, 5f, 5m, 5n, 5o, and 5p). The Verwey transition is nearly absent, and no transitions are evident in the ZFC-FC curves (Figures 5n and 5p). No LT transition has been observed in magnetization derivative curves in Z-II and Z-IV samples, which is consistent with the presence of greigite (Figures 5f, 5n, and 5p; Chang et al., 2009; Roberts et al., 2011).

3.2.3. FORC Diagrams

In addition to diagnostic room- and low-temperature magnetic measurements, FORC diagrams were obtained to provide information about magnetic minerals and domain states of samples from cores NGHP-01-05C and NGHP-01-07B. Representative FORC diagrams for the four sediment zones of cores NGHP-01-05C and NGHP-01-07B are shown in Figures 6a–6h. FORC distributions for most of the samples are characterized by a peak at $B_C \sim 10$ with closed contours that are indicative of the dominance of vortex state behavior in magnetite (Lascu et al., 2018; Muxworthy & Dunlop, 2002; Roberts et al., 2000, 2017; Figure 6a–6h). FORC distributions for samples from Z-IV (i.e., at BSR depth) of cores NGHP-01-05C and NGHP-01-07B are also indicative of vortex state ($B_C \sim 10$–15 mT) magnetite (Figures 6g–6h).

3.3. Mineralogical Analyses of Magnetic Particles

SEM-EDS analyses support our rock magnetic observations and confirm that titanomagnetite is the dominant magnetic mineral in the studied sediments. Detrital ferrimagnetic iron oxides and diagenetic magnetic iron sulfide minerals of various sizes are observed in all sediment cores (Figures 7a–7l). Z-I contains well-preserved, fresh, and less altered titanomagnetite grains. EDS data for these grains indicate the presence of iron, titanium, and oxygen with minor traces of silicon, calcium, potassium, manganese, aluminum, and vanadium (Figures 7a, 7e, and 7i). Diagenetically formed pyrite crystals occur as individual grains and as aggregates in the magnetically weak zone (Z-II). EDS data indicate the presence of sulfur and iron along with minor amounts of calcium, phosphorous, aluminium, and silicon (Figures 7b, 7f, and 7j).
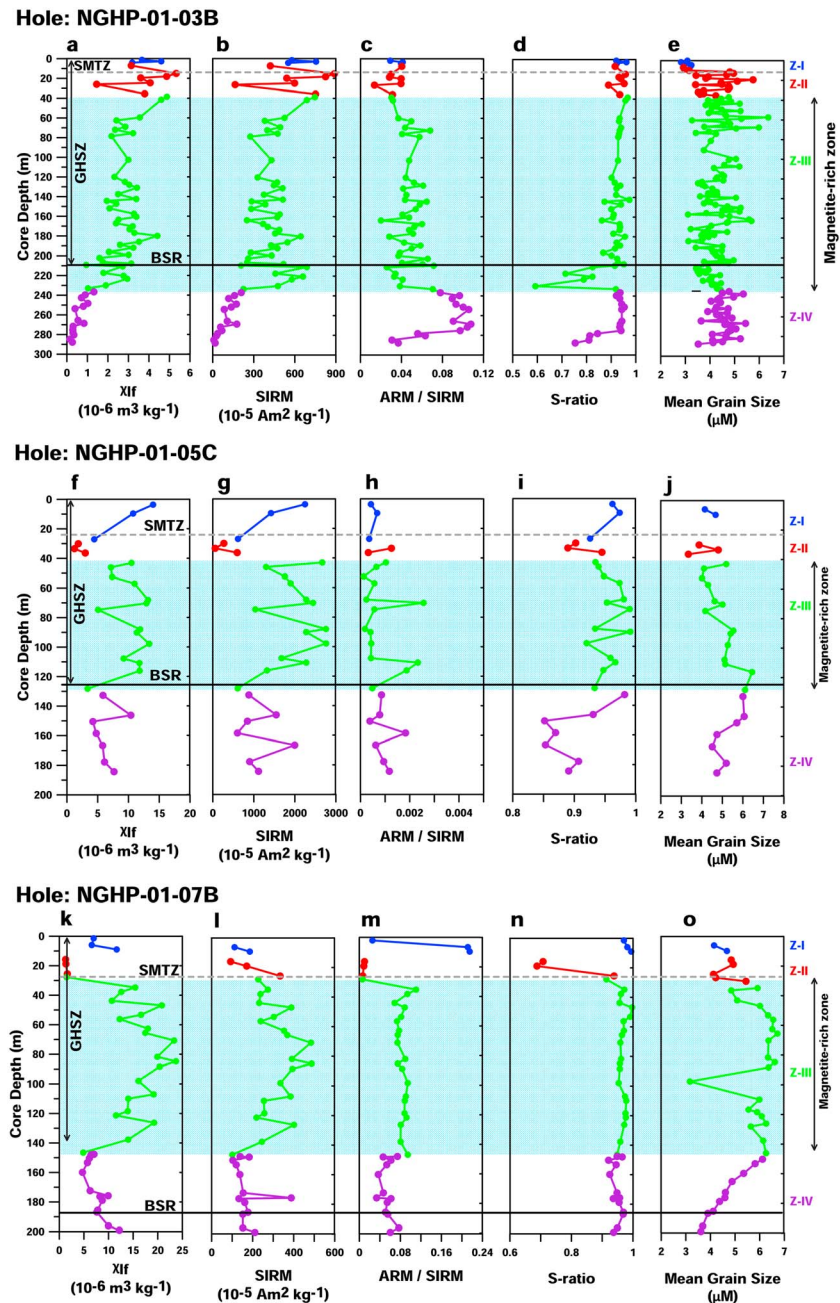
Figure 3. Depth variations of selected magnetic and sediment grain size data for sediment cores (a–e) NGHP-01-03B, (f–j) NGHP-01-05C, and (k–o) NGHP-01-07B. Data from discrete samples are color-coded (zone-I: dark blue, zone-II: red, zone-III: green, zone-IV: purple) according to the sedimentary magneto-zones demarcated based on magnetic susceptibility variations. Increased magnetic susceptibility in zone-III is highlighted by a blue shading. The depths of the bottom simulating reflector (BSR), sulfate-methane transition zone (SMTZ), and the gas hydrate stability zone (GHSZ) are marked. ARM = anhysteretic remanent magnetization, SIRM = saturation isothermal remanent magnetization.

In magnetically enhanced zone (Z-III), we observed numerous titanomagnetite and pyrite grains with various sizes and shapes. The titanomagnetite grains showed evidence of corrosion related to diagenetic alteration (Figures 7c, 7g, and 7k). EDS data indicate a dominance of iron, titanium, and sulfur with traces of phosphorous, calcium, silicon, potassium, and manganese (Figures 7c, 7g, and 7k). In addition to discrete Fe-Ti rich magnetic particles, numerous titanohematite particles with pyrite growths were found in this zone. Skeletal titanohematite lamellae (Figure S1a), pyrite overgrowths on titanomagnetite grains
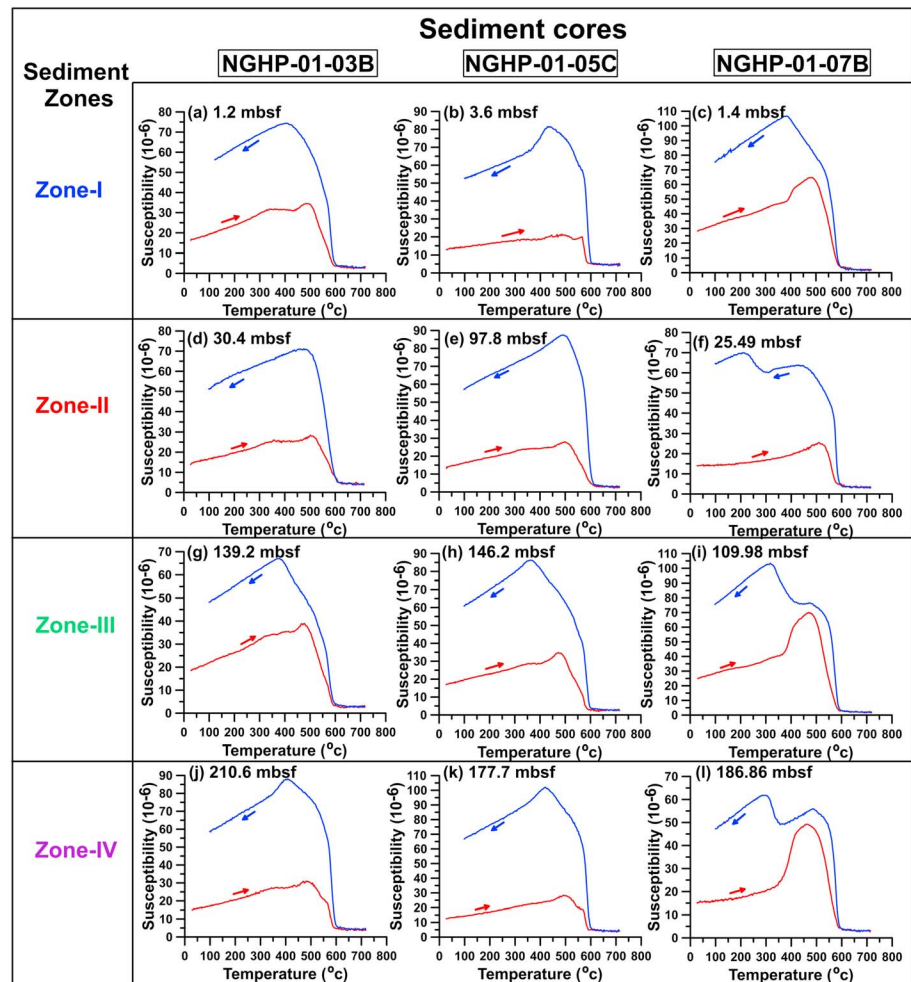
Figure 4. Temperature dependence of magnetic susceptibility (χ-T) for selected representative samples from the four sediment zones of the three studied sediment cores NGHP-01-03B, NGHP-01-05C, and NGHP-01-07B. Solid red lines indicate heating curves, and blue lines indicate cooling curves.

(Figure S1b), and well-preserved titanomagnetite grains are observed (Figure S1c). Z-IV (i.e., below the present-day BSR) contains a mixture of titanomagnetite and pyrite grains (Figures 7d, 7h, and 7l). EDS results reveal the presence of sulfur, iron, and titanium with minor traces of calcium, silicon, aluminum, and manganese (Figures 7d, 7h, and 7l).

3.4. X-Ray Diffraction Analysis on Magnetic Separates

Titanomagnetite is also identified in X-ray diffraction (XRD) results as the dominant magnetic mineral in all sediment zones (Figures 8). XRD data confirm the presence of pyrite in zones with reduced magnetic susceptibility (Z-II and Z-IV; Figures 8b, 8d, 8f, 8h, 8j, and 7l). Pyrite is also present in the magnetically enhanced zone (Z-III) in all three studied sediment cores (NGHP-01-03B, NGHP-01-05C, and NGHP-01-07B; Figures 8c, 8g, and 8k).

3.5. Correlation Between Magnetic and Geochemical Parameters

As previously documented by Badesab et al. (2017) in core NGHP-01-10D, a positive relationship between χ_{lf} and SIRM is observed in all analyzed cores, but with different slopes for different mineral types (Figure 9a). Two distinct groupings are evident. Samples from core NGHP-01-07B have higher χ_{lf} and low SIRM compared to cores NGHP-01-03B and NGHP-01-05C, which have linear relationships between χ_{lf} and SIRM (Figure 9a). Magnetite concentration (χ_{lf}) variations are large, while high χ_{lf} and lower χ_{fd}% values suggest the dominance of coarser magnetic grains (Figure 9b). χ_{fd} largely varies from 0% to ~6% (Figure 9b).
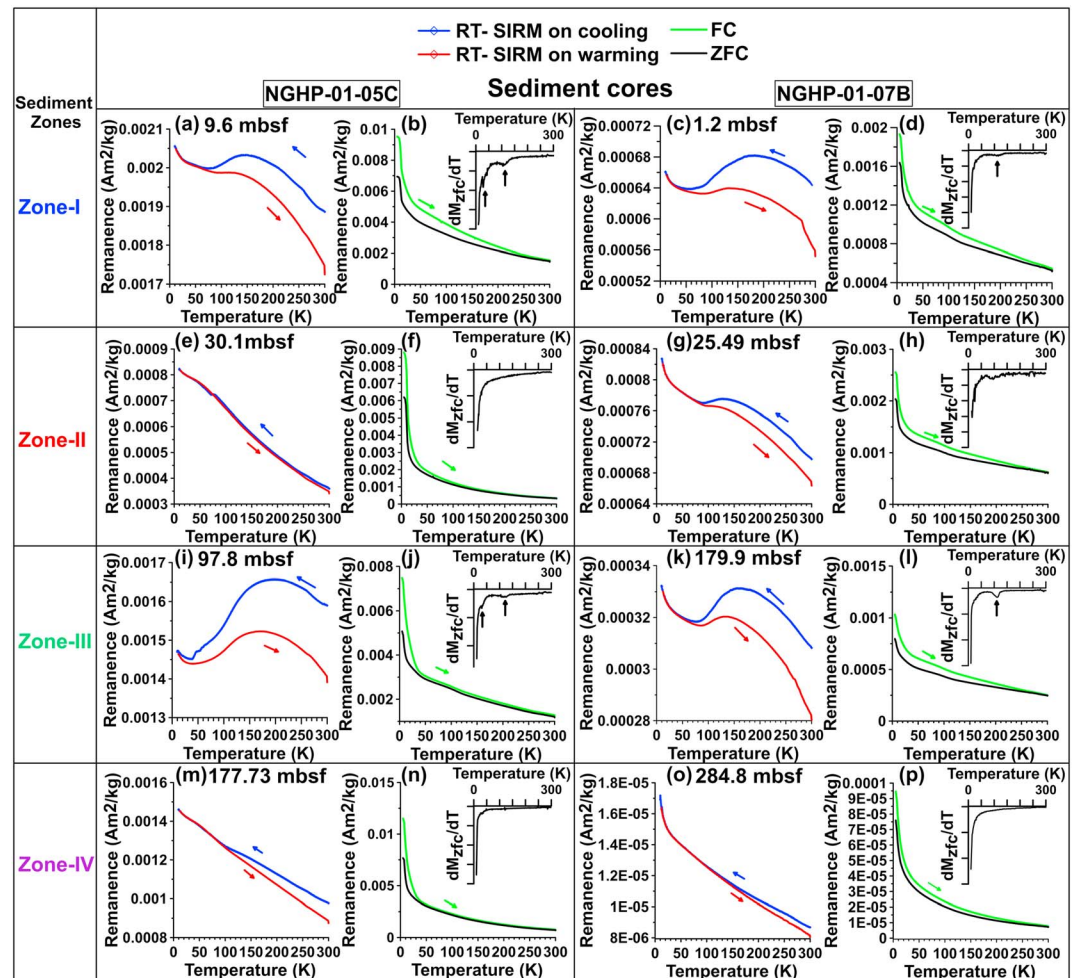
Figure 5. Low-temperature (< 300 K) magnetization curves for representative samples from the four sediment zones identified in sediment cores NGHP-01-05C and NGHP-01-07B. A distinct Verwey transition (for magnetite) and Besnus transition (for detrital pyrrhotite) is observed in the studied samples from different zones. FC = field-cooled, RT-SIRM = saturation isothermal remanent magnetization at room temperature, ZFC = zero field-cooled.

Lower values for some samples that have higher χ_{fd} value reflect a finer grain size trend for a subset of the data (Figure 9b).

SIRM/χ_{lf} versus χ_{lf} trends have proven to be diagnostic of identifying different magnetic mineral types in gas hydrate bearing sediments (Larrasoaña et al., 2007). The analyzed samples are categorized into three subgroups (Figure 9c). Samples with low SIRM/χ_{lf} and higher χ_{lf} values indicate the dominance of magnetite. Lower χ_{lf} and wide-ranging SIRM/χ_{lf} values suggest the presence of ferrimagnetic iron sulfides. Data that fall within the intermediate range of χ_{lf} and SIRM/χ_{lf} values represent mixtures of magnetite and magnetic iron sulfides (Figure 9c).

As indicated above, the bulk magnetic mineralogy is dominated by vortex state titanomagnetite. The source of magnetic mineral assemblages can be differentiated by δ_{ZFC} and δ_{FC} as proposed by Moskowitz et al. (1993). δ_{FC}/δ_{ZFC} values are close to 1, which indicates that the titanomagnetites are detrital (Figure 9d; Moskowitz et al., 1993; Housen & Moskowitz, 2006). All data cluster according to mineralogy and fall on a 1:1 line. Samples with low δ_{ZFC} and δ_{FC} (<0.18) represent the ferrimagnetic iron sulfides, while high δ_{ZFC} and δ_{FC} values (>0.4) correspond to magnetite (Figure 9d; Kars & Kodama, 2015a, 2015ab).

Negative correlation between χ_{lf} and CRS is observed for cores MD161/Stn8, MD161/Stn13, and NGHP-01-10D, which lie near cores NGHP-01-03B and NGHP-01-05C from this study and overlie methane hydrate deposits from the K-G basin (Figures 1 and 9e). A clear trend of reducing χ_{lf} with increasing CRS is
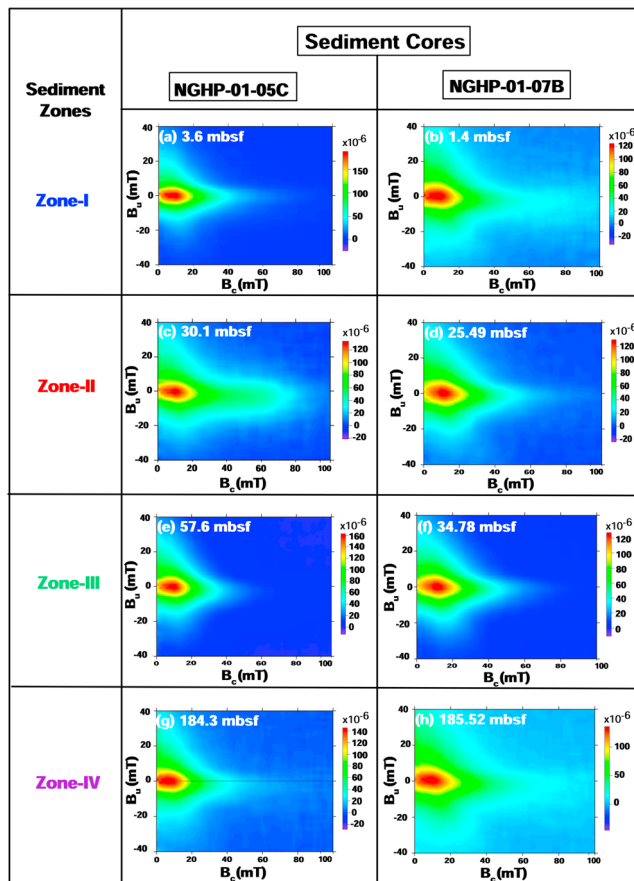
Figure 6. Representative first-order reversal curve diagrams for the four sedimentary magnetozones from cores NGHP-01-05C and NGHP-01-07B. All results are indicative of ferrimagnetic iron oxides, that is, titanomagnetite in the vortex state (Lascu et al., 2018; Roberts et al., 2017).

suggested here to be a proxy for identifying the paleomethane seepage events in gas hydrate forming environments as documented by Badesab et al. (2017).

4. Discussion

We examined the magnetic and sedimentological signatures of three sediment cores to evaluate the influence of sedimentary, tectonic, and diagenetic processes on the development of a fracture-filled gas hydrate system in the K-G basin. We explore these influences below.

4.1. Controls on Supply of Magnetic Minerals to the K-G Basin

Changes in monsoons, Himalayan uplift, weathering intensities, erosional processes in peninsular India, and glacial/interglacial cycles influenced the supply of detrital particles to the K-G basin (Curray et al., 1982; Colin et al., 1999; Krishna et al., 2016; Rao & Kessarkar, 2001; Sangode et al., 2001; Weber et al., 1997). The K-G basin receives a large sediment load from peninsular India through the Krishna and Godavari rivers. These rivers drain through the Deccan Traps basalts and Precambrian metamorphic rocks and deliver sediments from these terrains into the K-G basin (Ramesh & Subramanian, 1988). Sediment cores NGHP-01-10D, NGHP-01-03B, NGHP-01-05C, and NGHP-01-07B from the K-G basin preserve a record of sedimentary processes in the basin. Downcore magnetic property and sediment grain size variations are interpreted to indicate different controls on magnetic mineral supply into the K-G basin. Almost uniform and enhanced magnetic susceptibilities in Z-III in all studied cores may be attributed to multiple mass transport deposits (MTDs) as observed in the K-G basin (Figures 2a–2d, 3a–3o, and S2). Titanomagnetite is the most abundant magnetic mineral in Deccan basalts (Sangode et al., 2001) and fluvial sediments from peninsular India. The Krishna and Godavari Rivers have much higher magnetite contents compared to those sourced from the Himalayan regions (Sager & Hall, 1990; Phillips et al., 2014; Prajith et al., 2018; Sangode et al., 2001, 2007). Magnetic, XRD and SEM results indicate the dominance of well-preserved coarse titanomagnetite grains in zone-III (Figures 3a–3o, 4g-4i, 5i–5l, 7c, 7g, 7k, 8c, 8g, and 8k). These observations suggest that detrital magnetic particles in Z-III are sourced from Deccan basalts and were mainly supplied during periods of high sedimentation through peninsular river systems. χ_{lf} fluctuations within Z-III provide indications of multiple short-term higher sedimentation events in the K-G basin (Figures 2a–2d, 3a, 3f, 3k, and S2). They also indicate that in the rapidly depositing sedimentary system of the K-G basin, magnetic susceptibility scanning of sediment cores has the potential to detect subtle variations in detrital sediment inputs into marine basins.

MTDs are found commonly on the continental slopes, in channel-levee systems, and in basin-floor settings, for example, in Kumano Basin, Nankai Trough, Japan, the West African margin, North Sea, Gulf of Mexico, and the Californian and Brazilian margins (Moore et al., 2015; Shanmugam et al., 1994, 1995; Shanmugam, 2006). In the K-G basin, multiple MTDs have been identified in shallow (Ramana et al., 2007; Ramprasad et al., 2011) and deep offshore regions (Yamamoto et al., 2018), as confirmed by high-resolution seismic reflection data, multibeam bathymetry, seafloor topography, physical properties, lithology, and sediment ages (Ramprasad et al., 2011; Yamamoto et al., 2018). Recent studies demonstrate that neotectonic events, gas hydrate dissociation, sea level variations, and rapid sedimentation events can trigger slumping/sliding to produce MTDs in the K-G basin (Ramana et al., 2007, Ramprasad et al., 2011). High-resolution seismic records of sites NGHP-01-10D, NGHP-01-03B, and NGHP-01-05C indicate the presence of multiple acoustically transparent layers with no internal reflections that are typical of MTDs and indicate that the deposits are formed instantaneously (Figure S2; Anitha et al., 2014; Pratson & Laine, 1989; Ramprasad et al., 2011). The subbottom profiler data from the K-G basin indicate the occurrence of Holocene and pre-Holocene
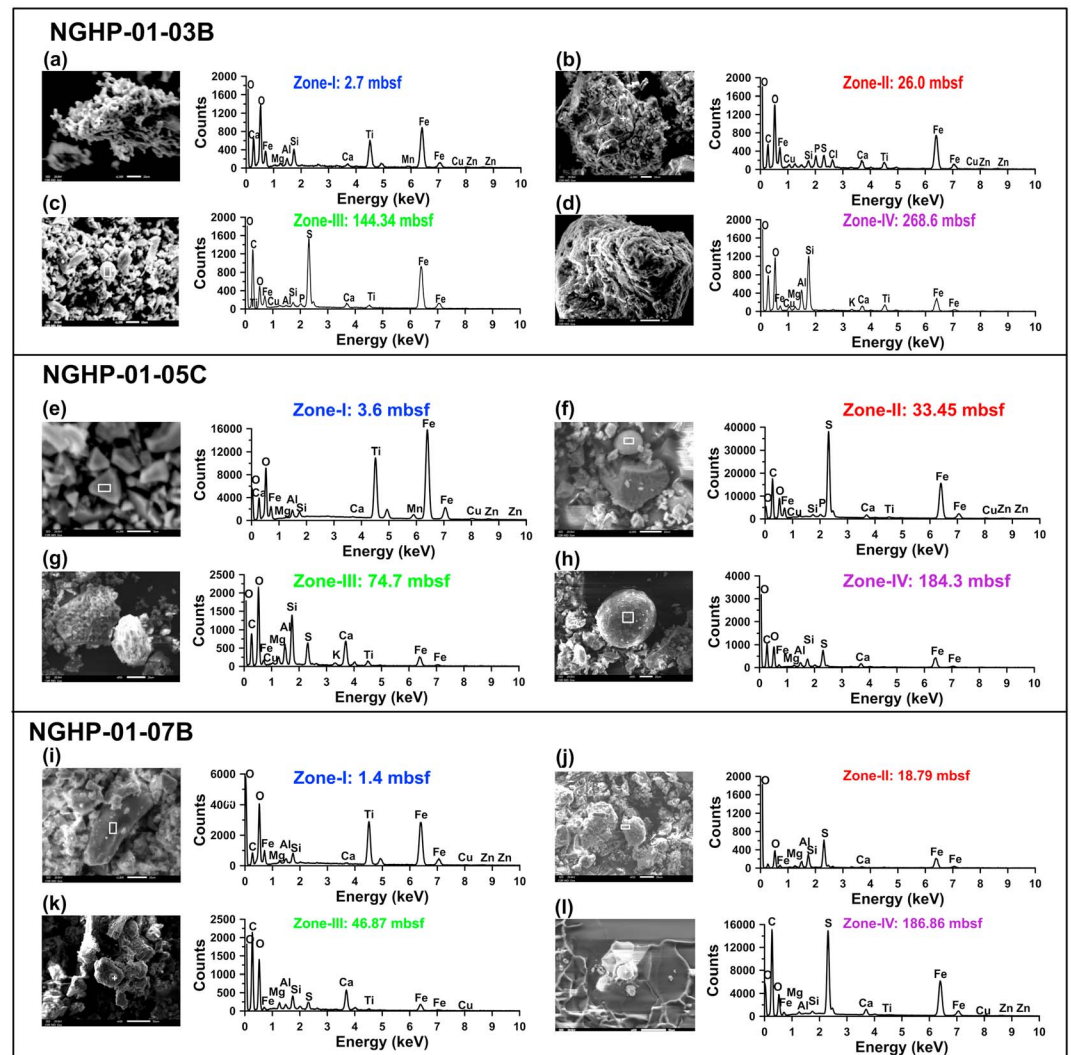
Figure 7. Scanning electron microscope images (secondary electron) on magnetic extracts from different sediment zones of NGHP-01-03B, NGHP-01-05C, and NGHP-01-07B. Energy dispersive X-ray spectroscopy spectra are placed adjacent to the respective images (a–l). Iron (Fe), titanium (Ti), sulfur (S), oxygen (O), calcium (Ca), silicon (Si), carbon (C), aluminum (Al), magnesium (Mg), potassium (K), zinc (Zn), and manganese (Mn) peaks are indicated.

MTDs, which are overlain by finely layered sediments (Dewangan et al., 2011; Mazumdar et al., 2012; Ramana et al., 2007; Ramprasad et al., 2011). A distinct band of enhanced magnetic susceptibility (Z-III) in core NGHP-01-10D reported by Badesab et al. (2017) appears to be a larger extensive feature throughout the K-G basin as seen in cores NGHP-01-05C and NGHP-01-07B (Figures 2a–2d). Mazumdar et al. (2012) provided a direct indication for slumping and mass transportation of deposits as evident by the age reversal in ^{14}C AMS dates observed in sediment cores from the K-G basin. We propose that the magnetically enhanced and laterally extensive band of Z-III observed in all four cores represents several MTDs that may have been generated by more rapid sedimentation events in slope regions of the K-G basin that were later buried to form a distinct and magnetically enhanced sediment magnetic property zone (Z-III) as evident at all four sediment cores (Figures 2a–2d, 3a, 3f, 3k, and S2). Such repeated MTDs contributed to produce an overall higher sedimentation rate interval in the K-G basin.

4.2. Linkages Between Shale Tectonics, High Sedimentation Events, and Gas Hydrate Formation in the K-G Basin

Gravity-driven shale tectonics governs the formation of shale bulges and toe-thrust structures in the K-G basin (Choudhuri et al., 2010), which host major gas hydrate deposits (Dewangan et al., 2010). The spatial
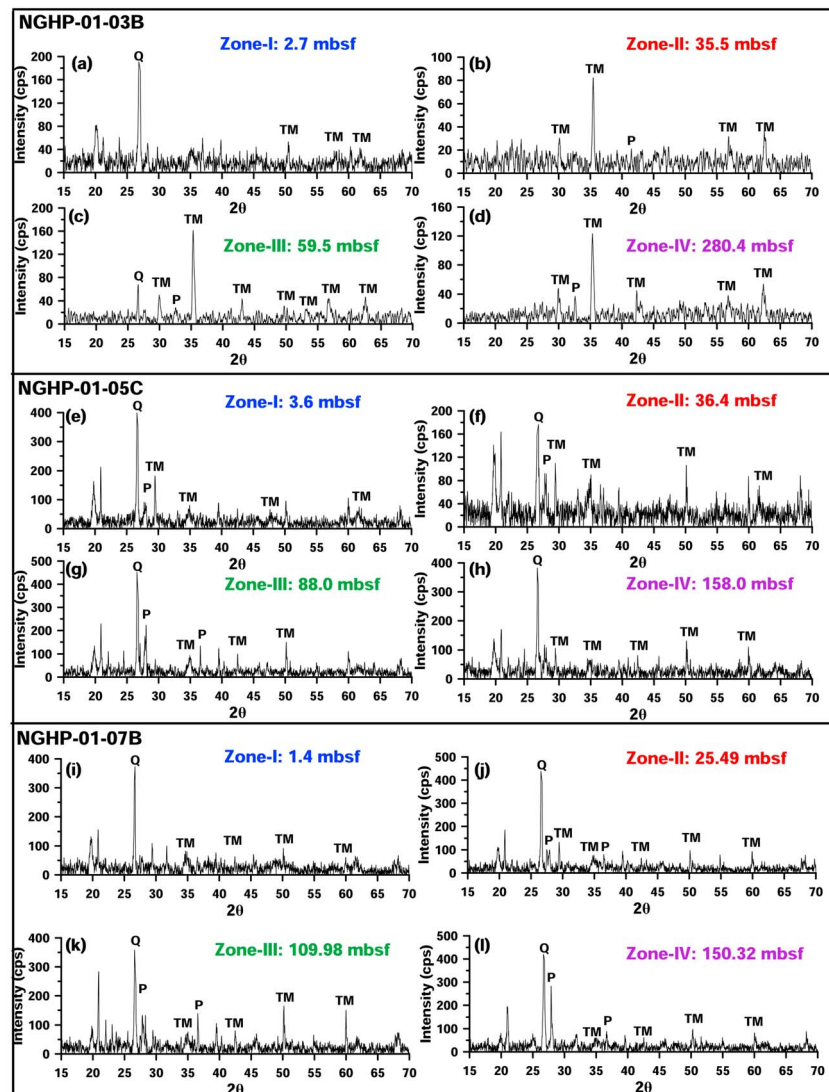
Figure 8. X-ray diffraction spectra for minerals extracted from different sediment zones of cores (a–d) NGHP-01-03B, (e–h) NGHP-01-05C, and (i–l) NGHP-01-07B. TM = titanomagnetite, P = pyrite, Q = quartz.

and temporal distribution of these structures depends on tectonic events and sediment depocenters in the basin over geological timescales. Rapid deposition of Miocene sediments after establishment of the monsoon system at ~24 Myr (Clift et al., 2008) led to the formation of overpressured shale strata in the K-G basin. The movement of mobile shale strata resulted in numerous growth faults in the upper shelf and upper slope regions with proximal and distal shale bulges in the middle slope and rise regions (Choudhuri et al., 2010). The proximal shale bulges continued to grow during the Pliocene due to ongoing sedimentation in the shelf region while distal bulges ceased to grow during this period. Increased sediment flux at 0.8 Ma due to increased deformation in the Himalayas (Clift et al., 2005) led to the formation of mega depocenters in the shelf region (Krishna et al., 2016). We propose that this increased late Pleistocene sedimentation might have accentuated the shale bulge growth, which appears as bathymetric mounds on the seafloor. These mounds are potential locations for gas hydrate formation (Dewangan et al., 2010).

We now attempt to link magnetic properties with neotectonic events in the K-G basin. Magnetic minerals supply, transportation, and burial in marine sediments are controlled by climatic, tectonic, and hydrodynamic forcing, and hence, χ_{lf} variations can provide clues about sedimentary processes and depositional environments (Hatfield & Maher, 2008, 2009; Oldfield et al., 1985). In the K-G basin, shale tectonism has
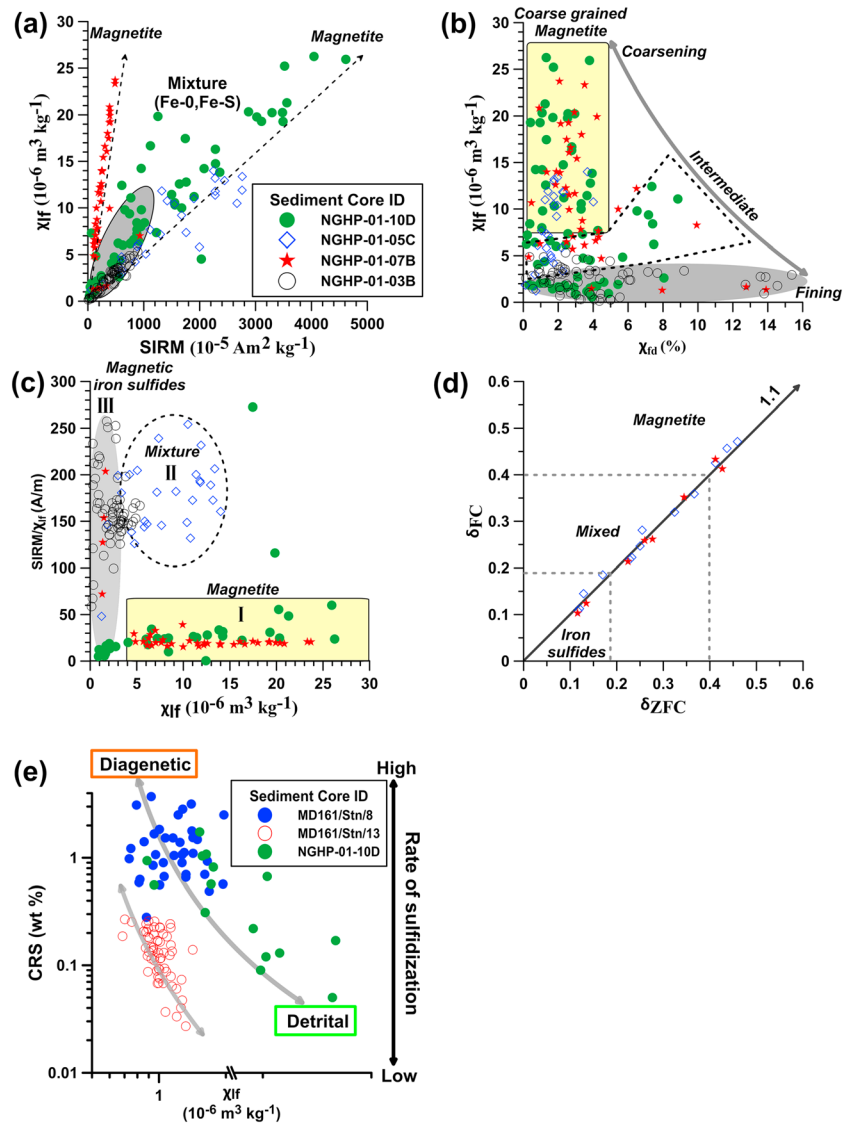
Figure 9. (a–c) Scatterplots of magnetic parameters (χ, saturation isothermal remanent magnetization (SIRM), $\chi_{fd}\%$, SIRM/χ, and anhysteretic remanent magnetization (ARM)/SIRM) for cores NGHP-01-10D, NGHP-01-03B, NGHP-01-05C, and NGHP-01-07B. (d) δ_{FC} versus δ_{ZFC} derived from low-temperature measurements (Moskowitz et al., 1993) for cores NGHP-01-05C and NGHP-01-07B. (e) Plot of chromium reducible sulfur (CRS) versus χ_{lf} for sediment cores NGHP-01-10D, MD161/Stn-8, and MD161/Stn-13. Note that gray arrows in the scatter plots are used to highlight trends. Magnetic and CRS data for sediment cores NGHP-01-10D, MD161/Stn-8, and MD161/Stn-13 are from Badesab et al. (2017) and Peketi et al. (2012, 2015).

led to the development of faults, fractures, mounds, and ridges on the seafloor. Sediment cores NGHP-01-10D and NGHP-01-5C lie on a mound, and the observed magnetically enhanced Z-III in both cores appears to represent the former shale bulges that formed as a result of shale strata movement (Figure 2; Choudhuri et al., 2010; Dewangan et al., 2010).

Later, as sedimentation increased during the Pleistocene, this region was exposed to rapid uplift and faulting as a result of shale-tectonism that was triggered by rapid sediment loading (Dewangan et al., 2010; Krishna et al., 2016). Highly pressurized strata were generated as a result of higher sedimentation rates that triggered growth of faults, folds, and upthrusting features (bathymetric mounds and ridges) in the K-G basin. These structures likely acted as conduits for upward fluid/gas migration to enter the gas hydrate stability zone (Dewangan et al., 2010; Shankar & Riedel, 2010). A fivefold late Pleistocene sedimentation rate increase in the K-G basin (Krishna et al., 2016) led to the generation of large MTDs that were deposited rapidly

and provided the pressure and temperature conditions needed for gas hydrate nucleation (Figure S2). The highest gas hydrate saturations occur within magnetically enhanced Z-III in all studied cores (Figure 3; Collett et al., 2014; Kumar et al., 2014). Fault growth facilitated methane gas migration through magnetically enhanced Z-III, which led to the formation of huge gas hydrate deposits. Therefore, the observed magnetic property variations at the studied sites (NGHP-01-10D and NGHP-01-05C) are controlled largely by episodic flow of methane and sulfide-enriched fluids through the fracture network that formed as a result of shale tectonism. During periods of normal sedimentation (Z-II), gas hydrate accumulation along the fault system resulted in fault system closure (Badesab et al., 2017).

More rapid sedimentation and tectonic stress could increase significantly the pore-fluid pressure of highly pressurized strata, leading to fluid migration to shallower depths (Flemings et al., 2006, 2008; Yamamoto et al. 2007, 2009; Yamamoto & Kawakami, 2014). Increased pore pressure beyond the sediment shear strength could trigger methane-rich fluid expulsion/seepage events (Crémière et al., 2016; Karstens et al., 2018). Episodic methane seepage would lead to multiple events of AOM-coupled sulfate reduction to cause dissolution of primary magnetic mineral assemblages and precipitation of secondary magnetic iron sulfides to create a distinct sediment magnetic signature (Dewangan et al., 2013; Riedinger et al., 2005). A sudden χ_{lf} drop due to iron oxide dissolution and pyrite growth and enriched CRS within Z-III (Peketi et al., 2012) provide clues of multiple past methane seepage events triggered by short-term paleomethane expulsion events in the K-G basin similar to those observed in the continental margin offshore of Argentina and Uruguay (Riedinger et al., 2005). Previous multiproxy studies by Mazumdar et al. (2009) confirmed the occurence of paleomethane expulsion events at sites MD161/Stn 8 and MD161/Stn 13 (close to site-NGHP-01-10D). Hence, it is likely that shale tectonism induced by rapid sedimentation events played a key role in the evolution of the K-G basin gas hydrate system.

Differential sediment loading due to a Pliocene change in the direction and amount of sediment supply in the Bay of Bengal was driven by climatic and tectonic changes and resulted in a shift of sediment depocentres in the K-G basin (Choudhuri et al., 2010; Cullen, 1981; Prell et al., 1980; Sangode et al., 2007). Core NGHP-01-03B is located in a marginal slope basin that formed during recent shale bulge uplift and has low χ_{lf} and SIRM unlike cores NGHP-01-05C and NGHP-01-07B (Figures 2b, 3a, and 3b). We propose that core NGHP-01-03B was formerly a sediment depocenter dominated by mixed, poorly sorted, and weakly magnetic sediments as reflected by relatively low χ_{lf} and mixed sediment grain size in Z-III as compared to other cores NGHP-01-05C and NGHP-01-07B (Figures 3a, 3b, and 3e).

4.3. Diagenetic Alteration of Detrital Magnetic Minerals

Downcore variations in magnetic mineral concentration, grain size, and mineralogy in all studied cores seem to be largely affected by the identified rapid sedimentation events and by postdepositional sediment diagenesis induced by AOM-coupled sulfate reduction processes (Figures S2 and S3). Reduction of χ_{lf} with depth in Z-I is attributed to diagenetic transformation that resulted in primary detrital iron oxide dissolution and iron sulfide precipitation (Figures 2a–2d, 3a, 3f, 3k, 4a–4c, 7a, 7e, 7i, 8a, 8e, and 8i). A χ_{lf} decrease and the presence of pyrite within the sulfidic zone (Z-II), that is, the present depth of the SMTZ, are due to pyritization fuelled by enhanced AOM-coupled sulfate reduction (Figures 2a–2d, 7b, 7f, 7j, 8b, 8f, 8j, and S3). Increased sedimentation in K-G basin during sediment interval Z-III affected diagenetic processes and favored rapid burial to cause less alteration and enhanced preservation of detrital magnetic particles to create a magnetically enriched interval Z-III (Figure S2). Skeletal titanohematite grains in Z-III are indicative of diagenetic dissolution of the Fe-rich parts of the particle (Nowaczyk, 2011; Roberts, 2015) with Ti-rich parts being less reactive (Figure S1a). Higher T_v values in samples from Z-I and Z-III indicate the presence of detrital magnetite (Figures 5a–5d and 5i–5l; Chang, Heslop, et al., 2016). Z-IV lies below the present-day BSR and is marked by low χ_{lf} with the presence of magnetic iron sulfides that might have formed as a result of deep pyritization processes and that probably represent a fossil gas hydrate sedimentary interval as proposed by Badesab et al. (2017; Figures 7h, 7l, 8d, and 8l). This interpretation is similar to findings at Nankai Trough (Kars & Kodama, 2015a, 2015b) and Cascadia Margin (Housen & Musgrave, 1996; Larrasoaña et al., 2007).

Previous studies have reported the widespread occurrence of the magnetic iron sulfides, greigite (Fe_3S_4) and hexagonal pyrrhotite that formed authigenically in methane-rich and gas hydrate bearing sedimentary

environments at Hydrate Ridge, Cascadia Margin (Housen & Musgrave, 1996; Larrasoaña et al., 2007; Musgrave et al., 2006), Nankai Trough (Kars & Kodama, 2015a, 2015b), and the continental margin offshore of southwestern Taiwan (Horng, 2018; Horng & Roberts, 2018). The presence of gas hydrates enhances microbial activity that results mainly in ferrimagnetic greigite precipitation (Housen & Musgrave, 1996; Riedinger & Brunner, 2014). Microbiological studies by Cragg et al. (1996) in sediment cores from Cascadia margin observed that methane oxidation rates are enhanced within the gas hydrate zone and result in increased bacterial populations. The availability of methane to fuel microbiological activity during gas hydrate formation lead to iron sulfide precipitation from brine with high concentration of sulfide (Wellsbury et al., 2000). Larrasoaña et al. (2007) reported that in southern Hydrate Ridge, authigenic greigite and pyrrhotite formed as a byproduct of microbially mediated diagenetic reactions in the AOM and gas hydrate zone. We did not observe greigite here in the potential gas hydrate bearing sedimentary zone (Z-III and Z-IV). Dewangan et al. (2013) reported greigite in Z-II (17-23 mbsf) of a sediment core (MD161/Stn 8) close to core NGHP-01-10D. It is possible that greigite was formerly present in Z-II, Z-III, and Z-IV in the studied cores. Later, when conditions became disadvantageous for greigite formation/preservation due to gas hydrate dissociation caused by changing pressure-temperature or increased sedimentation (Housen & Musgrave, 1996; Karstens et al., 2018; Larrasoaña et al., 2007; Musgrave et al., 2006), ferrimagnetic greigite would have been subsequently transformed into paramagnetic pyrite in Z-II, Z-III, and Z-IV (Berner, 1984; Kao et al., 2004). Similar observations have been reported for a sediment core (Hole C0008C) from the megasplay fault zone of Nankai Trough (Kars & Kodama, 2015a, 2015ab). As evident from the XRD data, the presence of pyrite within magnetic mineral extracts from Z-II, Z-III, and Z-IV could also be due to the occurence of particles with a pyrite rim and greigite core (Figures 8b, 8c, 8d, 8f, 8g, 8j, 8k, and 8l; Ebert et al., 2018; Roberts & Turner, 1993). The common presence of quartz in magnetic mineral extracts from all zones could also be due to silicate-hosted magnetic mineral inclusions that are protected and survived diagenetic dissolution (Chang, Roberts, et al., 2016; Figure 8).

The presence of pyrrhotite has been reported widely in methane-rich sedimentary environments where high concentration of methane occur near disseminated gas hydrates (Jørgensen et al., 2004; Kars & Kodama, 2015a, 2015b; Larrasoaña et al., 2007; Neretin et al., 2004; Roberts et al., 2010). Hexagonal pyrrhotite (Fe_9S_{10} or $Fe_{11}S_{12}$) often forms authigenically in methanic sedimentary environments (Horng, 2018), while monoclinic pyrrhotite (ferrimagnetic; Fe_7S_8) is found widely in igneous and metamorphic rocks (Horng & Roberts, 2006; Horng et al., 2012; Horng & Huh, 2011; O'Reilly et al., 2000; Rochette et al., 2001, 2003) and can be eroded and transported through river systems to be deposited in marine environments. Low-temperature magnetic data indicate the presence of monoclinic pyrrhotite based on the presence of the Besnus transition at ~35 K in Z-III of core NGHP-01-05C (Figures 5i–5j). Horng and Roberts (2018) argued that detrital monoclinic pyrrhotite grains released from proximal sources (igneous or metamorphic sources) will exhibit a Besnus transition, while hexagonal pyrrhotite that is observed widely in methane-rich sediments offshore of southwestern Taiwan does not exhibit a Besnus transition. Deccan basalts and Precambrian metamorphic rocks in the hinterlands surrounding the K-G basin are potential sources of detrital pyrrhotite in the studied samples (Ramesh & Subramanian, 1988). Clay mineralogical studies have demonstrated that the peninsular rivers are the major supplier of sediments to the K-G basin (Mazumdar et al., 2015; Rao et al., 1988; Rao, 1991). Hence, the monoclinic pyrrhotite identified in the much wider gas hydrate bearing sediment magneto zone (Z-III) of Hole-NGHP-01-05C (Figures 5i–5j) is interpreted to have a detrital origin. The absence of LT transitions in magnetically reduced Z-II and Z-IV is consistent with the presence of iron sulfides (greigite and hexagonal pyrrhotite), which are commonly present in such methane-rich environments and do not exhibit a LT transition. In such cases, LT magnetic results do not provide clear magnetic mineral identifications, so other methods are needed to detect such minerals (Chang et al., 2009; Roberts et al., 2011; Figures 5f, 5n, and 5p).

4.4. Magnetic Susceptibility as a Proxy for Tracking Paleo-SMTZ and Methane Seepage Events in Marine Sediments

Past studies have demonstrated the potential of χ_{lf} as a proxy for identifying the SMTZ in continental margin sediments offshore of Argentina and Uruguay (Riedinger et al., 2005), southwestern Taiwan (Horng & Chen, 2006), rapidly deposited sediments offshore of North Island, New Zealand (Rowan & Roberts, 2006), coal-bearing sediments, offshore of Shimokita Peninsula, Japan (Phillips et al., 2017), the Argentine continental

slope (Garming et al., 2005), Nankai Margin, southwestern Japan (Kars & Kodama, 2015a, 2015b; Shi et al., 2017), Cascadia margin offshore of western North America (Housen & Musgrave, 1996; Larrasoaña et al., 2007), and Vestnesa Ridge, offshore of western Svalbard (Schneider et al., 2018; Sztybor & Rasmussen, 2017). The effects of higher sedimentation rates and sedimentary events (e.g., mass transport deposits) on the sediment geochemical record, especially for reconstructing past methane seepage events, are not well understood. The K-G basin is characterized by dynamic depositional conditions controlled by non-steady-state sedimentary processes (abrupt sedimentation changes), subsurface gas hydrate occurrence, paleomethane seepage events, sediment slumping/sliding, MTDs, and fault system growth induced by shale tectonics. Therefore, the K-G basin provides a suitable sedimentary environment to test the potential of magnetic susceptibility as a proxy for tracking paleo-SMTZ fronts in a complex marine sedimentary system (Dewangan et al., 2010; Mazumdar et al., 2009; Peketi et al., 2012, Ramana et al., 2009; Ramprasad et al., 2011; Shanmugam et al., 2009; Shankar & Riedel, 2010). A drop in χ_{lf} and SIRM and the presence of pyrite within the sulfidic zone (Z-II) are attributed to intense pyritization fuelled by AOM-coupled sulfate reduction at the present-day SMTZ (Figures 3a, 3f, 3k, 7b, 7f, 7j, 8b, 8f, 8j, and S3; Collett et al., 2008). Maintaining the SMTZ at specific sediment depths is governed by the upward-migrating methane flux, downward diffusion of sulfate, and sedimentation variations. In the AOM zone, the rate of χ_{lf} loss is determined by the contact time between iron-bearing minerals and reactive H_2S-rich fluids (Canfield & Berner, 1987; Canfield et al., 1992; Dewangan et al., 2013; Riedinger et al., 2005; Roberts & Turner, 1993). MTDs generated by rapid sedimentation events could significantly alter H_2S build-up at the SMTZ front and thereby reduce the contact time required for completion of diagenetic reactions that result in partial magnetic susceptibility loss as documented from the continental margin offshore of Argentina and Uruguay (Riedinger et al., 2005) and the K-G Basin (Badesab et al., 2017; Dewangan et al., 2013; Hong et al., 2014). The anomalous χ_{lf} increase and coarsening of magnetic grain size in Z-III of cores NGHP-01-10D, NGHP-01-03B, NGHP-01-05C, and NGHP-01-07B have been attributed to MTD complexes generated by higher sedimentation events in the K-G Basin (Figure 3 and S2). Distinct χ_{lf} drops at several depth intervals followed by the occurrence of pyrite and titanomagnetite grains within Z-III, that is, below the present-day SMTZ, provide clues about the temporal build-up and rapid migration of paleo-SMTZ fronts that were caused by short-lived AOM-coupled sulfate reduction activity affected by abrupt sedimentation (Figure 3 and S2). The intermitted occurrence of lower χ_{lf} within Z-III also hints at periods of decreased sedimentation rate that favored partial iron mineral dissolution through weakened pyritization. Therefore, it is likely that in the rapidly depositing K-G basin sedimentary system, sufficient methane concentrations and lower sedimentation rates are required for long-term sustenance of the SMTZ, which eventually created distinct χ_{lf} minima. However, in such a scenario, magnetic tracking could help to resolve subtle changes caused by short-term fluctuations in sediment supply and diagenesis.

Recent studies have demonstrated that in rapidly depositing methane-rich marine sedimentary environments, enrichment of CRS ($\delta^{34}S_{CRS}$) and molybdenum (Mo) can be used as proxies to identify paleo-SMTZs and methane seepage events in marine sediments (Chen et al., 2016; Hu et al., 2017; Li et al., 2016; Lin et al., 2016; Peketi et al., 2012, 2015). Negative correlation between CRS content and χ_{lf} in sediment cores MD161/Stn8, MD161/Stn13, and NGHP-01-10D (Figure 9e; Badesab et al., 2017) suggests that magnetic tracking in combination with geochemical proxies (CRS, $\delta^{34}S_{CRS}$, Mo) can be used to constrain paleo-SMTZ and methane seepage events in marine sediments.

4.5. Conceptual Magnetic Mineralogical Model to Constrain Gas Hydrate Evolution in K-G Basin

Based on the magnetic mineralogical signatures recorded in four sediment cores (NGHP-01-10D, NGHP-01-03B, NGHP-01-05C, and NGHP-01-07B), a conceptual model is proposed to constrain the influence of natural geological and sedimentary processes on the dynamics of the fracture-filled gas hydrate system of the K-G basin (Figures 10a–10d). Tectonic changes, erosion process in the Himalayan mountain ranges, and intensification of the Asian summer monsoon delivered a huge terrigenous sediment load to the K-G basin through activation of peninsular rivers that resulted in the formation of a deep gas reservoir (Colin et al., 1999; Chauhan et al., 1993, 2004; Krishna et al., 2016; Sangode et al., 2001; Weber et al., 1997). Higher sedimentation rate events resulted in the formation of local sediment depocentres (proximal) and shale bulges (distal; Choudhari et al., 2010), which coincide with magneto-zone Z-III. Highly pressurized sediment strata that developed as a result of continued rapid sedimentation events triggered growth of a fault system that
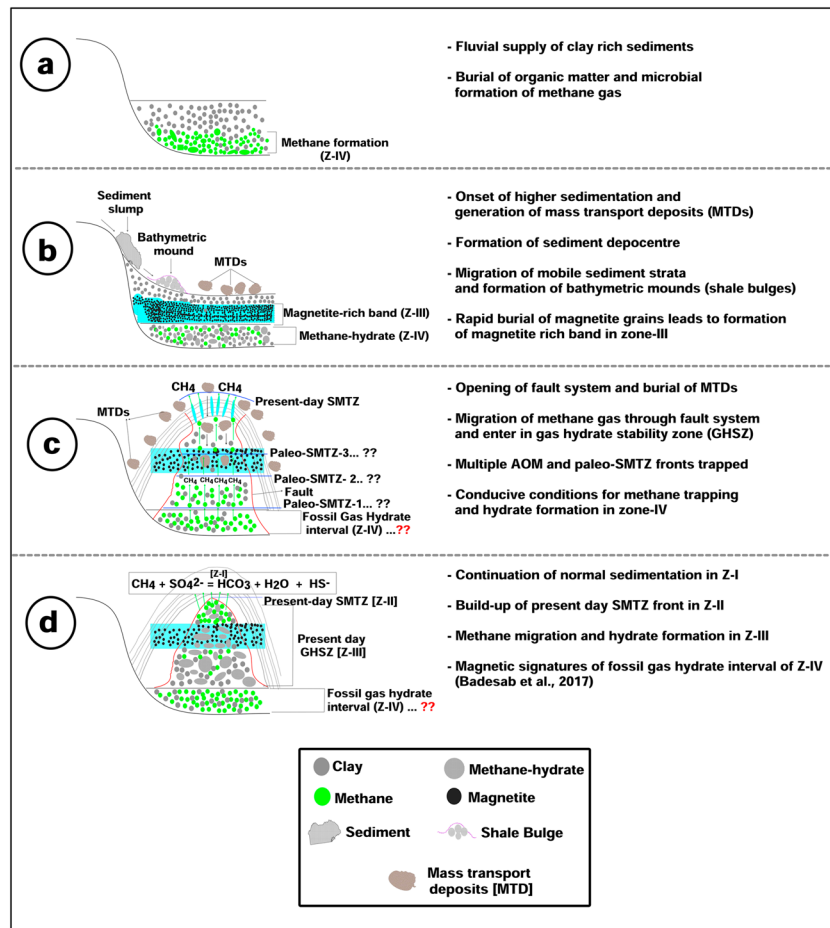
Figure 10. (a–d) Conceptual model for different controls (tectonic, sediment deposition, methane seepage dynamics, gas hydrates [formation/dissociation], and sediment diagenesis) on magnetic mineralogical variations observed in sediment cores NGHP-01-03B, NGHP-01-05C, and NGHP-01-07B. AOM = anaerobic oxidation of methane, SMTZ = sulfate-methane transition zone.

acted as a conduit for fluid/gas migration in Z-III. Fault growth facilitated trapping, burial, and preservation of magnetite-rich sediment, which along with the mass transport deposits formed the magnetically enhanced Z-III. As sedimentation continued, sediment pore pressure increased significantly, leading to the short-term expulsion and migration of methane-rich fluids through a fault network that generated local H_2S gradients produced as a result of AOM-coupled sulfate reduction in the vicinity of faults and fractures. When H_2S was abundant, as will be the case when methane fluxes are high, pyritization reactions proceeded to completion so that pyrite dominated over intermediate sulfides such as greigite, thereby creating distinct χ_{lf} drops in Z-III. Larrasoaña et al. (2007) showed this with extensive iron sulfide formation (mainly pyrite) occurring along faults and in their immediate vicinity. Pyrite aggregates formed along faults, which resulted in the diagenetic depletion of magnetic signals and potentially indicates paleo-SMTZ positions. Methane migration through the gas hydrate stability zone led to the nucleation of gas hydrates along the fault, which later acted as a seal for fault system closure and subsequent trapping of methane gas and hydrate in the K-G basin. Simultaneous sedimentation provided an impermeable seal for gas hydrate preservation in the K-G basin. Z-I represents the present-day sedimentary and geochemical environment of the K-G basin. Detrital iron-bearing minerals supplied through Indian river systems reacted with the H_2S generated by bacterial activity via organic matter decomposition and AOM-coupled sulfate reduction in Z-I to cause primary magnetic mineral dissolution and χ_{lf} decrease.

5. Conclusions

We present magnetic, geochemical, and sedimentological records from three sediment cores that overlie methane hydrate deposits in the K-G basin, offshore of India, Bay of Bengal. A linkage is evident between higher sedimentation events, magnetite enrichment, shale tectonism, and gas hydrate system development in the K-G basin. Relatively uniform and enhanced χ_{lf} values in Z-III for all studied cores reflect a period of higher sedimentation that had a dominant control on gas hydrate formation (Figure S2). Coarse titanomagnetite grains survived diagenesis because of rapid sedimentation and opening of a fault system that preserved a magnetic record of sedimentary processes, magnetic mineral diagenesis, and shale tectonism in K-G basin (Figure S2). The distinct magnetic susceptibility drop in gas hydrate stability zone (Z-III) and Z-IV helps to track paleo-SMTZ fronts and provide clues about rapid SMTZ shifts caused by short-term variability in methane fluxes and sedimentation rates.

Determination of precise timings of methane expulsion is difficult, but methane release might have started soon after fault system activation as evident by growth of pyrite aggregates induced by movement of H_2S-rich fluids through the fault/fracture network. Investigations of additional sediment cores from nearshore and shelf regions of the K-G basin is required to identify precisely the sediment depocenters and to detect sites of active cold seepage associated with shale bulges or sediment ridges. Our work demonstrates the potential use of magnetic mineralogical signatures to explore for gas hydrates in a highly dynamic and complex marine gas hydrate-bearing sedimentary system. A conceptual model is presented to explain the control of shale tectonism and rapid sedimentation on gas hydrate formation in the complex fracture-filled sedimentary system of the K-G basin (Figures 10a–10d). The magnetic mineralogical approach presented here has a wide scope and can be applied to other gas hydrate forming sedimentary environments.

References

Anitha, G., Ramana, M. V., Ramprasad, T., Dewangan, P., & Anuradha, M. (2014). Shallow geological environment of Krishna–Godavari offshore, eastern continental margin of India as inferred from the interpretation of high resolution sparker data. *Journal of Earth System Science*, *123*(2), 329–342.

Archer, D., & Buffett, B. (2005). Time-dependent response of the global ocean clathrate reservoir to climatic and anthropogenic forcing. *Geochemistry, Geophysics, Geosystems*, *6*, Q03002. https://doi.org/10.1029/2004GC000854

Badesab, F., Dewangan, P., Usapkar, A., Kocherla, M., Peketi, A., Mohite, K., et al. (2017). Controls on evolution of gas-hydrate system in the Krishna-Godavari basin, offshore India. *Geochemistry, Geophysics, Geosystems*, *18*, 52–74. https://doi.org/10.1002/2016GC006606

Bastia, R. (2007). *Geologic settings and petroleum systems of India's east coast offshore basins: Concepts and applications*. Bangalore, India: Technology Publications.

Berner, R. A. (1970). Sedimentary pyrite formation. *American Journal of Science*, *268*(1), 1–23.

Berner, R. A. (1984). Sedimentary pyrite formation: An update. *Geochimica et Cosmochimica Acta*, *48*(4), 605–615. https://doi.org/10.1016/0016-7037(84)90089-9

Biksham, G., & Subramanian, V. (1988). Sediment transport of the Godavari River basin and its controlling factors. *Journal of Hydrology*, *101*(1-4), 275–290. https://doi.org/10.1016/0022-1694(88)90040-6

Borowski, W. S., Paull, C. K., & Ussler, W. III (1996). Marine pore-water sulfate profiles indicate in situ methane flux from underlying gas hydrate. *Geology*, *24*(7), 655–658. https://doi.org/10.1130/0091-7613(1996)024<0655:MPWSPI>2.3.CO;2

Boswell, R., & Collett, T. S. (2011). Current perspectives on gas hydrate resources. *Energy and Environmental Science*, *4*(4), 1206–1215.

Canfield, D. E. (1989). Reactive iron in marine sediments. *Geochimica et Cosmochimica Acta*, *53*(3), 619–632. https://doi.org/10.1016/0016-7037(89)90005-7

Canfield, D. E., & Berner, R. A. (1987). Dissolution and pyritization of magnetite in anoxic marine sediments. *Geochimica et Cosmochimica Acta*, *51*(3), 645–659. https://doi.org/10.1016/0016-7037(87)90076-7

Canfield, D. E., Raiswell, R., & Bottrell, S. H. (1992). The reactivity of sedimentary iron minerals toward sulfide. *American Journal of Science*, *292*(9), 659–683. https://doi.org/10.2475/ajs.292.9.659

Chang, L., Heslop, D., Roberts, A. P., Rey, D., & Mohamed, K. J. (2016). Discrimination of biogenic and detrital magnetite through a double Verwey transition temperature. *Journal of Geophysical Research: Solid Earth*, *121*, 3–14. https://doi.org/10.1002/2015JB012485

Chang, L., Roberts, A. P., Heslop, D., Hayashida, A., Li, J., Zhao, X., et al. (2016). Widespread occurrence of silicate-hosted magnetic mineral inclusions in marine sediments and their contribution to paleomagnetic recording. *Journal of Geophysical Research: Solid Earth*, *121*, 8415–8431. https://doi.org/10.1002/2016JB013109

Chang, L., Roberts, A. P., Rowan, C. J., Tang, Y., Pruner, P., Chen, Q., & Horng, C. S. (2009). Low-temperature magnetic properties of greigite (Fe3S4). *Geochemistry, Geophysics, Geosystems*, *10*, Q01Y04. https://doi.org/10.1029/2008GC002276

Channell, J. E. T., & Hawthorne, T. (1990). Progressive dissolution of titanomagnetites at ODP Site 653 (Tyrrhenian Sea). *Earth and planetary science letters*, *96*(3-4), 469–480. https://doi.org/10.1016/0012-821X(90)90021-O

Chauhan, O. S., & Almeida, F. (1993). Influences of Holocene sea level, regional tectonics, and fluvial, gravity and slope currents induced sedimentation on the regional geomorphology of the continental slope off northwestern India. *Marine Geology*, *112*(1-4), 313–328. https://doi.org/10.1016/0025-3227(93)90176-V

Chauhan, O. S., Patil, S. K., & Suneethi, J.(2004). Fluvial influx and weathering history of the Himalayas since Last Glacial Maxima–isotopic, sedimentological and magnetic records from the Bay of Bengal. Current Science, 509-515. https://www.jstor.org/stable/24109183

Chen, F., Hu, Y., Feng, D., Zhang, X., Cheng, S., Cao, J., & Chen, D. (2016). Evidence of intense methane seepages from molybdenum enrichments in gas hydrate-bearing sediments of the northern South China Sea. *Chemical Geology*, *443*, 173–181. https://doi.org/10.1016/j.chemgeo.2016.09.029

Choudhuri, M., Guha, D., Dutta, A., Sinha, S., & Sinha, N. (2010). Spatio-temporal variations and kinematics of shale mobility in the Krishna-Godavari basin, India. In*: AAPG Hedberg Conference, Port of Spain*, Port of Spain,Trinidad and Tobago, 5–7 June 2006.

Clift, P. D., & Blusztajn, J. (2005). Reorganization of the western Himalayan river system after five million years ago. *Nature*, *438*(7070), 1001. https://doi.org/10.1038/nature04379

Clift, P. D., Hodges, K. V., Heslop, D., Hannigan, R., Van Long, H., & Calves, G. (2008). Correlation of Himalayan exhumation rates and Asian monsoon intensity. *Nature Geoscience*, *1*(12), 875. https://doi.org/10.1038/ngeo351

Colin, C., Turpin, L., Bertaux, J., Desprairies, A., & Kissel, C. (1999). Erosional history of the Himalayan and Burman ranges during the last two glacial–interglacial cycles. *Earth and Planetary Science Letters*, *171*(4), 647–660. https://doi.org/10.1016/S0012-821X(99)00184-3

Collett, T., Riedel, M., Cochran, J. R., Boswell, R., Presley, J., Kumar, P., et al., & the NGHP Expedition 01 Scientists (2008). Indian National Gas Hydrate Program, *Expedition - 01, Initial report*, Directorate General of Hydrocarbons, Ministry of Petroleum and Natural gas, India.

Collett, T. S., Boswell, R., Cochran, J. R., Kumar, P., Lall, M., Mazumdar, A., et al. (2014). Geologic implications of gas hydrates in the offshore of India: Results of the National Gas Hydrate Program Expedition 01. *Marine and Petroleum Geology*, *58*, 3–28. https://doi.org/10.1016/j.marpetgeo.2014.07.021

Cragg, B. A., Parkes, R. J., Fry, J. C., Weightman, A. J., Rochelle, P. A., & Maxwell, J. R. (1996). Bacterial populations and processes in sediments containing gas hydrates (ODP Leg 146: Cascadia Margin). *Earth and Planetary Science Letters*, *139*(3-4), 497–507. https://doi.org/10.1016/0012-821X(95)00246-9

Crémière, A., Lepland, A., Chand, S., Sahy, D., Condon, D. J., Noble, S. R., et al. (2016). Timescales of methane seepage on the Norwegian margin following collapse of the Scandinavian Ice Sheet. *Nature Communications*, *7*, 11509. https://doi.org/10.1038/ncomms11509

Cui, M., Wang, Z., Nageswara Rao, K., Sangode, S., Saito, Y., Chen, T., et al. (2017). A mid-to late-Holocene record of vegetation decline and erosion triggered by monsoon weakening and human adaptations in the south-east Indian Peninsula. *The Holocene*, *27*(12), 1976–1987. https://doi.org/10.1177/0959683617715694

Cullen, J. L. (1981). Microfossil evidence for changing salinity patterns in the Bay of Bengal over the last 20 000 years. *Palaeogeography, Palaeoclimatology, Palaeoecology*, *35*, 315–356. https://doi.org/10.1016/0031-0182(81)90101-2

Curray, J. R., Emmel, F. J., Moore, D. G., & Raitt, R. W. (1982). Structure, tectonics, and geological history of the northeastern Indian Ocean. In A. E. M. Nairn, & F. G. Stehli (Eds.), *The ocean basins and margins* (pp.399–450). Boston, MA: Springer. https://doi.org/10.1007/978-1-4615-8038-6_9

Dekkers, M. J. (1989). Magnetic properties of natural pyrrhotite. II. High- and low-temperature behaviour of Jrs and TRM as function of grain size. *Physics of the Earth and Planetary Interiors*, *57*, 266–283. https://doi.org/10.1016/0031-9201(89)90116-7

Dewangan, P., Basavaiah, N., Badesab, F. K., Usapkar, A., Mazumdar, A., Joshi, R., & Ramprasad, T. (2013). Diagenesis of magnetic minerals in a gas hydrate/cold seep environment off the Krishna–Godavari basin, Bay of Bengal. *Marine Geology*, *340*, 57–70. https://doi.org/10.1016/j.margeo.2013.04.016

Dewangan, P., Ramprasad, T., Ramana, M. V., Mazumdar, A., Desa, M., and Badasab, F. (2008). Shale tectonics in the continental slope and rise regions of Krishna-Godavari Basin, Bay of Bengal: Implication in gas-hydrate exploration. *In AGU Fall Meeting Abstracts*.

Dewangan, P., Ramprasad, T., Ramana, M. V., Mazumdar, A., Desa, M., & Badesab, F. K. (2010). Seabed morphology and gas venting features in the continental slope region of Krishna-Godavari basin, Bay of Bengal: Implications in gas-hydrate exploration. *Marine and Petroleum Geology*, *27*(7), 1628–1641. https://doi.org/10.1016/j.marpetgeo.2010.03.015

Dewangan, P., Sriram, G., Ramprasad, T., Ramana, M. V., & Jaiswal, P. (2011). Fault system and thermal regime in the vicinity of site NGHP-01-10, Krishna–Godavari basin, Bay of Bengal. *Marine and Petroleum Geology*, *28*, 1899–1914. https://doi.org/10.1016/j.marpetgeo.2011.03.009

Dickens, G. R., O'Neil, J. R., Rea, D. K., & Owen, R. M. (1995). Dissociation of oceanic methane hydrate as a cause of the carbon isotope excursion at the end of the Paleocene. *Paleoceanography and Paleoclimatology*, *10*(6), 965–971. https://doi.org/10.1029/95PA02087

Dunlop, D. J., Özdemir, Ö., & Schmidt, P. W. (1997). Paleomagnetism and paleothermometry of the Sydney Basin 2. Origin ofanomalously high unblocking temperatures. *Journal of Geophysical Research*, *102*(B12), 27,285–27,295. https://doi.org/10.1029/97JB02478

Ebert, Y., Shaar, R., Emmanuel, S., Nowaczyk, N., & Stein, M. (2018). Overwriting of sedimentary magnetism by bacterially mediated mineral alteration. *Geology*, *46*(4), 291–294. https://doi.org/10.1130/G39706.1

Enkin, R. J., Baker, J., Nourgaliev, D., Iassonov, P., & Hamilton, T. S. (2007). Magnetic hysteresis parameters and Day plot analysis to characterize diagenetic alteration in gas hydrate-bearing sediments. *Journal of Geophysical Research*, *112*, B06S90. https://doi.org/10.1029/2006JB004638

Esteban, L., Enkin, R. J., & Hamilton, T. (2008). Gas hydrates and magnetism: Comparative geological settings for diagenetic analysis. In *ICGH. Proceedings of the 6th International Conference on Gas Hydrates* (pp. 1-9).

Ferdelman, T. G., Fossing, H., Neumann, K., & Schulz, H. D. (1999). Sulfate reduction in surface sediments of the southeast Atlantic continental margin between 15 38′S and 27 57′S (Angola and Namibia). *Limnology and Oceanography*, *44*(3), 650–661. https://doi.org/10.4319/lo.1999.44.3.0650

Fleming, W. H., & Soner, H. M. (2006). *Controlled Markov processes and viscosity solutions*, (Vol. 25). Springer Science & Business Media.

Flemings, P. B., Long, H., Dugan, B., Germaine, J., John, C. M., Behrmann, J. H., et al. (2008). Pore pressure penetrometers document high over pressure near the seafloor where multiple submarine landslides have occurred on the continental slope, offshore Louisiana, Gulf of Mexico. *Earth and Planetary Science Letters*, *269*(3), 309–325. https://doi.org/10.1016/j.epsl.2007.12.005

Froelich, P., Klinkhammer, G. P., Bender, M. L., Luedtke, N. A., Heath, G. R., Cullen, D., et al. (1979). Early oxidation of organic matter in pelagic sediments of the eastern equatorial Atlantic: Suboxic diagenesis. *Geochimica et Cosmochimica Acta*, *43*(7), 1075–1090. https://doi.org/10.1016/0016-7037(79)90095-4

García-Tortosa, F. J., Alfaro, P., Gibert, L., & Scott, G. (2011). Seismically induced slump on an extremely gentle slope (<1) of the Pleistocene Tecopa paleolake (California). *Geology*, *39*(11), 1055–1058. https://doi.org/10.1130/G32218.1

Garming, J. F. L., Bleil, U., & Riedinger, N. (2005). Alteration of magnetic mineralogy at the sulfate–methane transition: Analysis of sediments from the Argentine continental slope. *Physics of the Earth and Planetary Interiors*, *151*(3-4), 290–308. https://doi.org/10.1016/j.pepi.2005.04.001

Goto, S., Matsubayashi, O., & Nagakubo, S. (2016). Simulation of gas hydrate dissociation caused by repeated tectonic uplift events. *Journal of Geophysical Research: Solid Earth*, *121*, 3200–3219. https://doi.org/10.1002/2015JB012711

Harrison, R. J., & Feinberg, J. M. (2008). FORCinel: An improved algorithm for calculating first order reversal curve distributions using locally weighted regression smoothing. *Geochemistry, Geophysics, Geosystems*, 9, Q05016. https://doi.org/10.1029/2008GC001987

Hatfield, R. G., & Maher, B. A. (2008). Suspended sediment characterization and tracing using a magnetic fingerprinting technique: Bassenthwaite Lake, Cumbria, UK. *Holocene*, 18, 105–115. https://doi.org/10.1177/0959683607085600

Hatfield, R. G., & Maher, B. A. (2009). Holocene sediment dynamics in an upland temperate lake catchment: Climaticand land-use impacts in the English Lake District. *Holocene*, 19, 427–438. https://doi.org/10.1177/0959683608101392

Herbozo, G., Hübscher, C., Kaul, N., Wagner, M., Pecher, I., & Kukowski, N. (2013). Influence of recent depositional and tectonic controls on marine gas hydrates in Trujillo Basin, Peru Margin. *Marine Geology*, 340, 30–48. https://doi.org/10.1016/j.margeo.2013.04.010

Hirt, A. M., & Gehring, A. U. (1991). Thermal alteration of the magnetic mineralogy in ferruginous rocks. *Journal of Geophysical Research*, 96(B6), 9947–9953. https://doi.org/10.1029/91JB00573

Hirt, A. M., Lowrie, W., Clendenen, W. S., & Kligfield, R. (1993). Correlation of strain and the anisotropy of magnetic susceptibility in the Onaping Formation: evidence for a near-circular origin of the Sudbury basin. *Tectonophysics*, 225(4), 231–254. https://doi.org/10.1016/0040-1951(93)90300-9

Hong, W. L., Solomon, E. A., & Torres, M. E. (2014). A kinetic-model approach to quantify the effect of mass transport deposits on pore water profiles in the Krishna–Godavari Basin, Bay of Bengal. *Marine and Petroleum Geology*, 58, 223–232. https://doi.org/10.1016/j.marpetgeo.2014.06.014

Horng, C. S. (2018). Unusual Magnetic Properties of Sedimentary Pyrrhotite in Methane-Seepage Sediments: Comparison with Metamorphic Pyrrhotite and Sedimentary Greigite. *Journal of Geophysical Research: Solid Earth.*, 123, 4601–4617. https://doi.org/10.1002/2017JB015262

Horng, C. S., & Chen, K. H. (2006). Complicated magnetic mineral assemblages in marine sediments offshore southwestern Taiwan: Possible influences of methane flux on the early diagenetic process. *Terrestrial, Atmospheric and Oceanic Sciences*, 17, 1009–1026. https://doi.org/10.3319/TAO.2006.17.4.1009(GH)

Horng, C.-S., & Huh, C.-A. (2011). Magnetic properties as tracers for source-to-sink dispersal of sediments: A case study in the Taiwan Strait. *Earth and Planetary Science Letters*, 309, 141–152. https://doi.org/10.1016/j.epsl.2011.07.002

Horng, C.-S., Huh, C.-A., Chen, K.-H., Lin, C.-H., Shea, K.-S., & Hsiung, K.-H. (2012). Pyrrhotite as a tracer for denudation of the Taiwan orogen. *Geochemistry,Geophysics, Geosystems*, 13, Q08Z47. https://doi.org/10.1029/2012GC004195

Horng, C. S., & Roberts, A. P. (2006). Authigenic or detrital origin of pyrrhotite in sediments? Resolving a paleomagnetic conundrum. *Earth and Planetary Science Letters*, 241(3-4), 750–762. https://doi.org/10.1016/j.epsl.2005.11.008

Horng, C. S., & Roberts, A. P. (2018). The low-temperature Besnus magnetic transition: Signals due to monoclinic and hexagonal pyrrhotite. *Geochemistry, Geophysics, Geosystems*, 19, 3364–3375. https://doi.org/10.1029/2017GC007394

Housen, B. A., & Moskowitz, B. M. (2006). Depth distribution of magnetofossils in near-surface sediments from the Blake/Bahama Outer Ridge, western North Atlantic Ocean, determined by low-temperature magnetism. *Journal of Geophysical Research*, 111, G01005. https://doi.org/10.1029/2005JG000068

Housen, B. A., & Musgrave, R. J. (1996). Rock-magnetic signature of gas hydrates in accretionary prism sediments. *Earth and Planetary Science Letters*, 139(3-4), 509–519. https://doi.org/10.1016/0012-821X(95)00245-8

Hu, Y., Chen, L., Feng, D., Liang, Q., Xia, Z., & Chen, D. (2017). Geochemical record of methane seepage in authigenic carbonates and surrounding host sediments: A case study from the South China Sea. *Journal of Asian Earth Sciences*, 138, 51–61. https://doi.org/10.1016/j.jseaes.2017.02.004

Hustoft, S., Bünz, S., Mienert, J., & Chand, S. (2009). Gas hydrate reservoir and active methane-venting province in sediments on < 20 Ma young oceanic crust in the Fram Strait, offshore NW-Svalbard. *Earth and Planetary Science Letters*, 284(1-2), 12–24. https://doi.org/10.1016/j.epsl.2009.03.038

Jahren, A. H., Conrad, C. P., Arens, N. C., Mora, G., & Lithgow-Bertelloni, C. (2005). A plate tectonic mechanism for methane hydrate release along subduction zones. *Earth and Planetary Science Letters*, 236(3-4), 691–704. https://doi.org/10.1016/j.epsl.2005.06.009

Johnson, J. E., & Phillips, S. C. (2014). Reconstructing paleo-SMT positions on the Cascadia margin using magnetic susceptibility. *Final Scientific Report, Univ. of New Hampshire, Durham, NH (United States)*.

Johnson, J. E., Phillips, S. C., Torres, M. E., Piñero, E., Rose, K. K., & Giosan, L. (2014). Influence of total organic carbon deposition on the inventory of gas hydrate in the Indian continental margins. *Marine and Petroleum Geology*, 58, 406–424. https://doi.org/10.1016/j.marpetgeo.2014.08.021

Jørgensen, B. B. (1982). Mineralization of organic matter in the sea bed—The role of sulphate reduction. *Nature*, 296(5858), 643–645. https://doi.org/10.1038/296643a0

Jørgensen, B. B., Böttcher, M. E., Lüschen, H., Neretin, L. N., & Volkov, I. I. (2004). Anaerobic methane oxidation and a deep H_2S sink generate isotopically heavy sulfides in Black Sea sediments. *Geochimica et Cosmochimica Acta*, 68(9), 2095–2118. https://doi.org/10.1016/j.gca.2003.07.017

Kao, S. J., Horng, C. S., Roberts, A. P., & Liu, K. K. (2004). Carbon–sulfur–iron relationships in sedimentary rocks from southwestern Taiwan: Influence of geochemical environment on greigite and pyrrhotite formation. *Chemical Geology*, 203(1-2), 153–168. https://doi.org/10.1016/j.chemgeo.2003.09.007

Karlin, R., & Levi, S. (1983). Diagenesis of magnetic minerals in recent haemipelagic sediments. *Nature*, 303(5915), 327. https://doi.org/10.1038/303327a0

Kars, M., & Kodama, K. (2015a). Authigenesis of magnetic minerals in gas hydrate bearing sediments in the Nankai Trough, Offshore Japan. *Geochemistry, Geophysics, Geosystems*, 16, 947–961. https://doi.org/10.1002/2014GC005614

Kars, M., & Kodama, K. (2015b). Rock magnetic characterization of ferrimagnetic iron sulfides in gas hydrate-bearing marine sediments at Site C0008, Nankai Trough, Pacific Ocean, off-coast Japan. *Earth, Planets and Space*, 67(1), 118. https://doi.org/10.1186/s40623-015-0287-y

Karstens, J., Haflidason, H., Becker, L. W., Berndt, C., Rüpke, L., Planke, S., et al. (2018). Glacigenic sedimentation pulses triggered post-glacial gas hydrate dissociation. *Nature Communications*, 9(1), 635. https://doi.org/10.1038/s41467-018-03043-z

Kasten, S., Freudenthal, T., Gingele, F. X., & Schulz, H. D. (1998). Simultaneous formation of iron-rich layers at different redox boundaries in sediments of the Amazon deep-sea fan. *Geochimica et Cosmochimica Acta*, 62, 2253–2264. https://doi.org/10.1016/S0016-7037(98)00093-3

Kasten, S., Zabel, M., Heuer, V., & Hensen, C. (2003). Processes and signals of nonsteady-state diagenesis in deep-sea sediments and their pore waters. In *The South Atlantic in the Late Quaternary*, (pp. 431–459). Berlin, Heidelberg: Springer. https://doi.org/10.1016/j.gca.2007.08.019

Kennett, J. P., Cannariato, K. G., Hendy, I. L., & Behl, R. J. (2000). Carbon isotopic evidence for methane hydrate instability during Quaternary interstadials. *Science*, *288*(5463), 128–133. https://doi.org/10.1126/science.288.5463.128

Knittel, K., & Boetius, A. (2009). Anaerobic oxidation of methane: Progress with an unknown process. *Annual Review of Microbiology*, *63*, 311–334. https://doi.org/10.1038/296643a0

Krishna, K. S., Ismaiel, M., Srinivas, K., Gopala Rao, D., Mishra, J., & Saha, D. (2016). Sediment pathways and emergence of Himalayan source material in the Bay of Bengal. *Current Science*, *110*. https://doi.org/10.18520/cs/v110/i3/363-372

Kumar, P., Collett, T. S., Boswell, R., Cochran, J. R., Lall, M., Mazumdar, A., et al. (2014). Geologic implications of gas hydrates in the offshore of India: Krishna-Godavari Basin, Mahanadi Basin, Andaman Sea, Kerala–Konkan Basin. *Marine and Petroleum Geology*, *58*, 29–98. https://doi.org/10.1016/j.marpetgeo.2014.07.031

Kvenvolden, K. A. (1988). Methane hydrate—A major reservoir of carbon in the shallow geosphere? *Chemical Geology*, *71*(1-3), 41–51. https://doi.org/10.1016/0009-2541(88)90104-0

Kvenvolden, K. A. (1993). Gas hydrates—Geological perspective and global change. *Reviews of Geophysics*, *31*(2), 173–187. https://doi.org/10.1029/93RG00268

Larrasoaña, J. C., Roberts, A. P., Musgrave, R. J., Gràcia, E., Piñero, E., Vega, M., & Martínez-Ruiz, F. (2007). Diagenetic formation of greigite and pyrrhotite in gas hydrate marine sedimentary systems. *Earth and Planetary Science Letters*, *261*(3-4), 350–366. https://doi.org/10.1016/j.epsl.2007.06.032

Lascu, I., Einsle, J. F., Ball, M. R., & Harrison, R. J. (2018). The vortex state in geologicmaterials: A micromagnetic perspective. *Journal of Geophysical Research: Solid Earth*, *123*, 7285–7304. https://doi.org/10.1029/2018JB015909

Leslie, B. W., Hammond, D. E., Berelson, W. M., & Lund, S. P. (1990). Diagenesis in anoxic sediments from the California continental borderland and its influence on iron, sulfur, and magnetite behaviour. *Journal of Geophysical Research*, *95*, 4453–4470. https://doi.org/10.1029/JB095iB04p04453

Li, N., Feng, D., Chen, L., Wang, H., & Chen, D. (2016). Using sediment geochemistry to infer temporal variation of methane flux at a cold seep in the South China Sea. *Marine and Petroleum Geology*, *77*, 835–845. https://doi.org/10.1016/j.marpetgeo.2016.07.026

Lin, Q., Wang, J., Taladay, K., Lu, H., Hu, G., Sun, F., & Lin, R. (2016). Coupled pyrite concentration and sulfur isotopic insight into the paleo sulfate–methane transition zone (SMTZ) in the northern South China Sea. *Journal of Asian Earth Sciences*, *115*, 547–556. https://doi.org/10.1016/j.jseaes.2015.11.001

Mazumdar, A., Dewangan, P., Joäo, H.M., Peketi, A.,Khosla, V.R., Kocherla, M., et al., (2009). Evidence of paleo–cold seep activity from the Bay of Bengal, offshore India. *Geochemistry,Geophysics, Geosystems*, *10*Q06005. https://doi.org/10.1029/2008GC002337

Mazumdar, A., Joao, H. M., Peketi, A., Dewangan, P., Kocherla, M., Joshi, R. K., & Ramprasad, T. (2012). Geochemical and geological constraints on the composition of marine sediment pore fluid: Possible link to gas hydrate deposits. *Marine and Petroleum Geology*, *38*(1), 35–52. https://doi.org/10.1016/j.marpetgeo.2012.07.004

Mazumdar, A., Kocherla, M., Carvalho, M. A., Peketi, A., Joshi, R. K., Mahalaxmi, P., et al. (2015). Geochemical characterization of the Krishna–Godavari and Mahanadi offshore basin (Bay of Bengal) sediments: a comparative study of provenance. *Marine and Petroleum Geology*, *60*, 18–33. https://doi.org/10.1016/j.marpetgeo.2014.09.005

Milkov, A. V., & Sassen, R. (2002). Economic geology of offshore gas hydrate accumulations and provinces. *Marine and Petroleum Geology*, *19*(1), 1–11. https://doi.org/10.1016/S0264-8172(01)00047-2

Moore, G. F., Boston, B. B., Strasser, M., Underwood, M. B., & Ratliff, R. A. (2015). Evolution of tectono-sedimentary systems in the Kumano Basin, Nankai Trough forearc. *Marine and Petroleum Geology*, *67*, 604–616. https://doi.org/10.1016/j.marpetgeo.2015.05.032

Moskowitz, B. M., Frankel, R. B., & Bazylinski, D. A. (1993). Rock magnetic criteria for the detection of biogenic magnetite. *Earth and Planetary Science Letters*, *120*(3-4), 283–300. https://doi.org/10.1016/0012-821X(93)90245-5

Musgrave, R. J., Bangs, N. L., Larrasoaña, J. C., Gràcia, E., Hollamby, J. A., & Vega, M. E. (2006). Rise of the base of the gas hydrate zone since the last glacial recorded by rock magnetism. *Geology*, *34*(2), 117–120. https://doi.org/10.1130/G22008.1

Muxworthy, A. R., & Dunlop, D. J. (2002). First-order reversal curve (FORC) diagrams for pseudo-single-domain magnetites at high temperature. *Earth and Planetary Science Letters*, *203*(1), 369–382. https://doi.org/10.1016/S0012-821X(02)00880-4

Muxworthy, A. R., & McClelland, E. (2000). Review of the low-temperature magnetic properties of magnetite from a rock magnetic perspective. *Geophysical Journal International*, *140*(1), 101–114. https://doi.org/10.1046/j.1365-246x.2000.00999.x

Neretin, L. N., Böttcher, M. E., Jørgensen, B. B., Volkov, I. I., Lüschen, H., & Hilgenfeldt, K. (2004). Pyritization processes and greigite formation in the advancing sulfidization front in the upper Pleistocene sediments of the Black Sea 1. *Geochimica et Cosmochimica Acta*, *68*(9), 2081–2093. https://doi.org/10.1016/S0016-7037(03)00450-2

Novosel, I., Spence, G. D., & Hyndman, R. D. (2005). Reduced magnetization produced by increased methane flux at a gas hydrate vent. *Marine Geology*, *216*(4), 265–274. https://doi.org/10.1016/j.margeo.2005.02.027

Nowaczyk, N. R. (2011). Dissolution of titanomagnetite and sulphidization in sediments from Lake Kinneret, Israel. *Geophysical Journal International*, *187*(1), 34–44. https://doi.org/10.1111/j.1365-246X.2011.05120.x

Oldfield, F., Maher, B. A., Donoghue, J., & Pierce, J. (1985). Particle-size related, mineral magnetic source sediment linkages in the Rhode River catchment, Maryland, USA. *Journal of the Geological Society*, *142*, 1035–1046. https://doi.org/10.1144/gsjgs.142.6.1035

O'Reilly, W., Hoffmann, V., Chouker, A. C., Soffel, H. C., & Menyeh, A. (2000). Magnetic properties of synthetic analogues of pyrrhotite ore in the grain size range 1–24 μm. *Geophysical Journal International*, *142*(3), 669–683. https://doi.org/10.1046/j.1365-246x.2000.00169.x

Özdemir, Ö., Dunlop, D. J., & Moskowitz, B. M. (2002). Changes in remanence, coercivity and domain state at low temperature in magnetite. *Earth and Planetary Science Letters*, *194*(3-4), 343–358. https://doi.org/10.1016/S0012-821X(01)00562-3

Pan, Y. X., Zhu, R. X., Banerjee, S. K., Gill, J., & Williams, Q. (2000). Rock magnetic properties related to thermal treatment of siderite: Behavior and interpretation. *Journal of Geophysical Research*, *105*, 783–794. https://doi.org/10.1029/1999JB900358

Panieri, G., Graves, C. A., & James, R. H. (2016). Paleo-methane emissions recorded in foraminifera near the landward limit of the gas hydrate stability zone offshore western Svalbard. *Geochemistry, Geophysics, Geosystems*, *17*, 521–537. https://doi.org/10.1002/2015GC006153

Passier, H. D., De Lange, G. J., & Dekkers, M. J. (2001). Magnetic properties and geochemistry of the active oxidation front and the youngest sapropel in the eastern Mediterranean Sea. *Geophysical Journal International*, *145*(3), 604–614. https://doi.org/10.1046/j.0956-540x.2001.01394.x

Passier, H. F., & Dekkers, M. J. (2002). Iron oxide formation in the active oxidation front above sapropel S1 in the eastern Mediterranean Sea as derived from low-temperature magnetism. *Geophysical Journal International*, *150*(1), 230–240. https://doi.org/10.1046/j.1365-246X.2002.01704.x

Paull, C. K., Ussler, W., & Dillon, W. P. (1991). Is the extent of glaciation limited by marine gas-hydrates? *Geophysical Research Letters*, *18*(3), 432–434. https://doi.org/10.1029/91GL00351

Peketi, A., Mazumdar, A., Joao, H. M., Patil, D. J., Usapkar, A., & Dewangan, P. (2015). Coupled C–S–Fe geochemistry in a rapidly accumulating marine sedimentary system: Diagenetic and depositional implications. *Geochemistry, Geophysics, Geosystems*, *16*, 2865–2883. https://doi.org/10.1002/2015GC005754

Peketi, A., Mazumdar, A., Joshi, R. K., Patil, D. J., Srinivas, P. L., & Dayal, A. M. (2012). Tracing the paleo sulfate–methane transition zones and H2S seepage events in marine sediments: An application of C-S-Mo systematic. *Geochemistry, Geophysics, Geosystems*, *13*, Q10007. https://doi.org/10.1029/2012GC004288

Petersen, N., T. Von Dobeneck, & H. Vali (1986). Fossil bacterial magnetite in deep-sea sediments from the South Atlantic Ocean, *Nature*, *320*, 611–615. https://doi.org/10.1038/320611a0

Philips, S. C. (2018). Diagenetic degradation of paleoenvironmental signals in magnetic susceptibility in the northern Bay of Bengal, *The IRM Quarterly*, Winter 2017-2018, Vol. 27 No.4

Phillips, S. C., Johnson, J. E., Clyde, W. C., Setera, J. B., Maxbauer, D. P., Severmann, S., & Riedinger, N. (2017). Rock magnetic and geochemical evidence for authigenic magnetite formation via iron reduction in coal-bearing sediments offshore Shimokita Peninsula, Japan (IODP Site C0020). *Geochemistry, Geophysics, Geosystems*, *18*, 2076–2098. https://doi.org/10.1002/2017GC006943

Phillips, S. C., Johnson, J. E., Giosan, L., & Rose, K. (2014). Monsoon-influenced variation in productivity and lithogenic sediment flux since 110 ka in the offshore Mahanadi Basin, northern Bay of Bengal. *Marine and Petroleum Geology*, *58*, 502–525. https://doi.org/10.1016/j.marpetgeo.2014.05.007

Pike, C. R., Roberts, A. P., & Verosub, K. L. (1999). Characterizing interactions in fine magnetic particle systems using first order reversal curves. *Journal of Applied Physics*, *85*(9), 6660–6667. https://doi.org/10.1063/1.370176

Prabhakar, K. N., & Zutshi, P. L. (1993). Evolution of southern part of Indian East Coast basin. *Journal of Geological Society of India*, *41*, 215–230.

Prajith, A., Tyagi, A., & Kurian, P. J. (2018). Changing sediment sources in the Bay of Bengal: Evidence of summer monsoon intensification and ice-melt over Himalaya during the Late Quaternary. *Palaeogeography, Palaeoclimatology, Palaeoecology*, *511*, 309–318. https://doi.org/10.1016/j.palaeo.2018.08.016

Pratson, L. F., & Laine, E. P. (1989). The relative importance of gravity-induced versus current-controlled sedimentation during the Quaternary along the Mideast U.S. outer continental margin revealed by 3.5 kHz echo character. *Marine Geology*, *89*, 87–126. https://doi.org/10.1016/0025-3227(89)90029-7

Prell, W. L., Hutson, W. H., Williams, D. F., Bé, A. W., Geitzenauer, K., & Molfino, B. (1980). Surface circulation of the Indian Ocean during the last glacial maximum, approximately 18,000 yr BP. *Quaternary Research*, *14*(3), 309–336. https://doi.org/10.1016/0033-5894(80)90014-9

Ramana, M. V., Ramprasad, T., Kamesh Raju, K. A., & Desa, M. (2007). Occurrence of gas hydrates along the continental margins of India, particularly the Krishna-Godavari off shore basin. *International Journal of Environmental Studies*, *64*(6), 675–693. https://doi.org/10.1080/00207230701476321

Ramana, M. V., Ramprasad, T., Paropkari, A. L., Borole, D. V., Rao, B. R., Karisiddaiah, S. M., & Gonsalves, M. J. (2009). Multidisciplinary investigations exploring indicators of gas hydrate occurrence in the Krishna–Godavari Basin offshore, east coast of India. *Geo-Marine Letters*, *29*(1), 25–38. https://doi.org/10.1007/s00367-008-0121-7

Ramesh, R., & Subramanian, V. (1988). Temporal, spatial and size variation in the sediment transport in the Krishna River basin, India. *Journal of Hydrology*, *98*, 53–65. https://doi.org/10.1016/0022-1694(88)90205-3

Ramprasad, T., Dewangan, P., Ramana, M. V., Mazumdar, A., Karisiddaiah, S. M., Ramya, E. R., & Sriram, G. (2011). Evidence of slumping/sliding in Krishna–Godavari offshore basin due to gas/fluid movements. *Marine and Petroleum Geology*, *28*(10), 1806–1816. https://doi.org/10.1016/j.marpetgeo.2011.02.007

Rao, G. N. (2001). Sedimentation, stratigraphy, and petroleum potential of Krishna-Godavari basin, East Coast of India. *American Association of Petroleum Geologists Bulletin*, *85*(9), 1623–1643.

Rao, V. P. (1991). Clay mineral distribution in the continental shelf sediments from Krishna to Ganges river mouth, east coast of India. *Indian Journal of Marine Sciences*, *20*, 7–12.

Rao, V. P., & Kessarkar, P. M. (2001). Geomorphology and geology of the Bay of Bengal and the Andaman Sea. In *The Indian Ocean: A Perspective* (Vol. 2, pp. 817–868). Bangalore, Karnataka, India: AA Balkema Publishers.

Rao, V. P., Reddy, N. P., & Rao, C. M. (1988). Clay mineral distribution in the shelf sediments off the northern part of the east coast of India. *Continental Shelf Research*, *8*(2), 145–151.

Riedel, M., Collett, T. S., & Shankar, U. (2011). Documenting channel features associated with gas hydrates in the Krishna–Godavari Basin, offshore India. *Marine Geology*, *279*(1-4), 1–11. https://doi.org/10.1016/j.margeo.2010.10.008

Riedinger, N., & Brunner, B. (2014). Data report: Concentration and sulfur isotope composition of iron monosulfide and pyrite from sediments collected during IODP Expedition 316. In M. Kinoshita, H. Tobin, J. Ashi, G. Kimura, S. Lallemant, E. J. Screaton, et al. (Eds.), Proc. IODP, 314/315/316. Washington, DC: Integrated Ocean Drilling Program Management International, Inc. https://doi.org/10.2204/iodp.proc.314315316.223.2014

Riedinger, N., Pfeifer, K., Kasten, S., Garming, J. F. L., Vogt, C., & Hensen, C. (2005). Diagenetic alteration of magnetic signals by anaerobic oxidation of methane related to a change in sedimentation rate. *Geochimica et Cosmochimica Acta*, *69*(16), 4117–4126. https://doi.org/10.1016/j.gca.2005.02.004

Roberts, A. P. (2015). Magnetic mineral diagenesis. *Earth-Science Reviews*, *151*, 1–47. https://doi.org/10.1016/j.earscirev.2015.09.010

Roberts, A. P., Almeida, T. P., Church, N. S., Harrison, R. J., Heslop, D., Li, Y., et al. (2017). Resolving the origin of pseudo-single domain magnetic behavior. *Journal of Geophysical Research: Solid Earth*, *122*, 9534–9558. https://doi.org/10.1002/2017JB014860

Roberts, A. P., Chang, L., Rowan, C. J., Horng, C. S., & Florindo, F. (2011). Magnetic properties of sedimentary greigite (Fe₃S₄): An update. *Reviews of Geophysics*, *49*, RG1002. https://doi.org/10.1029/2010RG000336

Roberts, A. P., Florindo, F., Larrasoaña, J. C., O'Regan, M. A., & Zhao, X. (2010). Complex polarity pattern at the former Plio–Pleistocene global stratotype section at Vrica (Italy): Remagnetization by magnetic iron sulphides. *Earth and Planetary Science Letters*, *292*(1-2), 98–111. https://doi.org/10.1016/j.epsl.2010.01.025

Roberts, A. P., Pike, C. R., & Verosub, K. L. (2000). First-order reversal curve diagrams: A new tool for characterizing the magnetic properties of natural samples. *Journal of Geophysical Research*, *105*(B12), 28,461–28,475. https://doi.org/10.1029/2000JB900326

Roberts, A. P., & Turner, G. M. (1993). Diagenetic formation of ferrimagnetic iron sulphide minerals in rapidly deposited marine sediments, South Island, New Zealand. *Earth and Planetary Science Letters*, *115*(1-4), 257–273. https://doi.org/10.1016/0012-821X(93)90226-Y

Roberts, A. P., Zhao, X., Harrison, R. J., Heslop, D., Muxworthy, A. R., Rowan, C. J., et al. (2018). Signatures of reductive magnetic mineral diagenesis from unmixing of first order reversal curves. *Journal of Geophysical Research: Solid Earth*, *123*, 4500–4522. https://doi.org/10.1029/2018JB015706

Rochette, P., Fillion, G., Ballou, R., Brunet, F., Ouladdiaf, B., & Hood, L. (2003). High pressure magnetic transition in pyrrhotite and impact demagnetization on Mars. *Geophysical Research Letters*, *30*(13), 1683. https://doi.org/10.1029/2003GL017359

Rochette, P., Fillion, G., Mattéi, J.-L., & Dekkers, M. J. (1990). Magnetic transition at 30–34 K in Fe7S8: Insight into a widespread occurrence of pyrrhotite in rocks. *Earth and Planetary Science Letters*, *98*, 319–328. https://doi.org/10.1016/0012-821X(90)90034-U

Rochette, P., Lorand, J. P., Fillion, G., & Sautter, V. (2001). Pyrrhotite and the remanent magnetization of SNC meteorites: A changing perspective on Martian magnetism. *Earth and Planetary Science Letters*, *190*, 1–12. https://doi.org/10.1016/S0012-821X(01)00373-9

Rowan, C. J., & Roberts, A. P. (2006). Magnetite dissolution, diachronous greigite formation, and secondary magnetizations from pyrite oxidation: Unravelling complex magnetizations in Neogene marine sediments from New Zealand. *Earth and Planetary Science Letters*, *241*(1-2), 119–137. https://doi.org/10.1016/j.epsl.2005.10.017

Rowan, C. J., Roberts, A. P., & Broadbent, T. (2009). Reductive diagenesis, magnetite dissolution, greigite growth and paleomagnetic smoothing in marine sediments: A new view. *Earth and Planetary Science Letters*, *277*(1-2), 223–235. https://doi.org/10.1016/j.epsl.2008.10.016

Sager, W. W., & Hall, S. A. (1990). 26. MAGNETIC PROPERTIES OF BLACK MUD TURBIDITES FROM ODP LEG 116, DISTAL BENGAL FAN, INDIAN OCEAN1.

Sangode, S. J., Sinha, R., Phartiyal, B., Chauhan, O. S., Mazari, R. K., Bagati, T. N., et al. (2007). Environmental magnetic studies on some quaternary sediments of varied depositional settings in the Indian sub-continent. *Quaternary International*, *159*, 102–118. https://doi.org/10.1016/j.quaint.2006.08.015

Sangode, S. J., Suresh, N., & Bagati, T. N. (2001). Godavari source in the Bengal fan sediments: Results from magnetic susceptibility dispersal pattern. *Current Science*, 660–664.

Schneider, A., Panieri, G., Lepland, A., Consolaro, C., Crémière, A., Forwick, M., et al. (2018). Methane seepage at Vestnesa Ridge (NW Svalbard) since the Last Glacial Maximum. *Quaternary Science Reviews*, *193*, 98–117. https://doi.org/10.1016/j.quascirev.2018.06.006

Shankar, U., & Riedel, M. (2010). Seismic and heat flow constraints from the gas hydrate system in the Krishna-Godavari basin, India. *Marine Geology*, *276*(1–4), 1–13. https://doi.org/10.1016/j.margeo.2010.06.006

Shanmugam, G. (2006). Deep-water processes and facies models: Implications for sandstone petroleum reservoirs. In *Handbook of petroleum exploration and production* (Vol. 5, pp. 270). Amsterdam, Netherlands: Elsevier.

Shanmugam, G., Bloch, R. B., Mitchell, S. M., Beamish, G. W., Hodgkinson, R. J., Damuth, J. E., et al. (1995). Basin-floor fans in the North Sea: sequence stratigraphic models vs. sedimentary facies. *American Association of Petroleum Geologists Bulletin*, *79*(4), 477–511.

Shanmugam, G., Lehtonen, L. R., Straume, T., Syvertsen, S. E., Hodgkinson, R. J., & Skibeli, M. (1994). Slump and debris-flow dominated upper slope facies in the Cretaceous of the Norwegian and northern North Seas (61–67 N): Implications for sand distribution. *American Association of Petroleum Geologists Bulletin*, *78*(6), 910–937.

Shanmugam, G., Shrivastava, S. K., & Das, B. (2009). Sandy debrites and tidalites of Pliocene reservoir sands in upperslope canyon environments, offshore Krishna–Godavari Basin (India): implications. *Journal of Sedimentary Research*, *79*(9), 736–756. https://doi.org/10.2110/jsr.2009.076

Shi, M., Wu, H., Roberts, A. P., Zhang, S., Zhao, X., Li, H., et al. (2017). Tectonic, climatic, and diagenetic control of magnetic properties of sediments from Kumano Basin, Nankai margin, southwestern Japan. *Marine Geology*, *391*, 1–12. https://doi.org/10.1016/j.margeo.2017.07.006

Sztybor, K., & Rasmussen, T. L. (2017). Diagenetic disturbances of marine sedimentary records from methane-influenced environments in the Fram Strait as indications of variation in seep in tensity during the last 35 000 years. *Boreas*, *46*(2), 212–228.

Tarduno, J. A., Sager, W. W., & Nogi, Y. (1995). Early cretaceous magnetostratigraphy and paleolatitudes from the mid-pacific mountains: Preliminary results bearing on guyot formation and pacific plate translation. In E. L. Winterer, W. W. Sager, J. V. Firth, & J. M. Sinton (Eds.), *Proc. ODP, Sci. Results*, (Vol. 143, pp. 395–398). College Station, TX: Ocean Drilling Program.

Thompson, R., & Oldfield, F. (1986). *Environmental magnetism*, (p. 227). London: Allen and Unwin.

Torres, M. E., Trehu, A. M., Cespedes, N., Kastner, M., Wortmann, U. G., Kim, J. H., et al. (2008). Methane hydrate formation in turbidite sediments of northern Cascadia, IODP Expedition 311. *Earth and Planetary Science Letters*, *271*, 170–180. https://doi.org/10.1016/j.epsl.2008.03.061

Treude, T., Niggemann, J., Kallmeyer, J., Wintersteller, P., Schubert, C. J., Boetius, A., & Jørgensen, B. B. (2005). Anaerobic oxidation of methane and sulfate reduction along the Chilean continental margin. *Geochimica et Cosmochimica Acta*, *69*(11), 2767–2779. https://doi.org/10.1016/j.gca.2005.01.002

Usapkar, A., Dewangan, P., Kocherla, M., Ramprasad, T., Mazumdar, A., & Ramana, M. V. (2014). Enhanced methane flux event and sediment dispersal pattern in the Krishna–Godavari offshore basin: Evidences from rock magnetic techniques. *Marine and Petroleum Geology*, *58*, 461–475. https://doi.org/10.1016/j.marpetgeo.2014.08.008

van Dongen, B. E., Roberts, A. P., Schouten, S., Jiang, W. T., Florindo, F., & Pancost, R. D. (2007). Formation of iron sulfide nodules during anaerobic oxidation of methane. *Geochimica et Cosmochimica Acta*, *71*, 5155–5167. https://doi.org/10.1016/j.gca.2007.08.019

Verosub, K. L., & Roberts, A. P. (1995). Environmental magnetism: Past, present, and future. *Journal of Geophysical Research*, *100*(B2), 2175–2192. https://doi.org/10.1029/94JB02713

Verwey, E. J. W. (1939). Electronic conduction of magnetite (Fe_3O_4) and its transition point at low temperatures. *Nature*, *144*(3642), 327. https://doi.org/10.1038/144327b0

von Huene, R., & Pecher, I. A. (1999). Vertical tectonics and the origins of BSRs along the Peru margin. *Earth and Planetary Science Letters*, *166*(1-2), 47–55. https://doi.org/10.1016/S0012-821X(98)00274-X

Wang, X., Hutchinson, D. R., Wu, S., Yang, S., & Guo, Y. (2011). Elevated gas hydrate saturation within silt and silty clay sediments in the Shenhu area, South China Sea. *Journal of Geophysical Research*, *116*, B05102. https://doi.org/10.1029/2010JB007944

Weber, M. E., Wiedicke, M. H., Kudrass, H. R., Hübscher, C., & Erlenkeuser, H. (1997). Active growth of the Bengal Fan during sea-level rise and highstand. *Geology*, *25*(4), 315–318. https://doi.org/10.1130/0091-7613(1997)025<0315:AGOTBF>2.3.CO;2

Wellsbury, P., Goodman, K., Cragg, B. A., & Parkes, R. J. (2000). The geomicrobiology of deep marine sediments from Blake Ridge containing methane hydrate (Sites 994, 995 and 997). In *Proceedings of the Ocean drilling program, Scientific results*, (Vol. 164, pp. 379–391). College Station, TX: Ocean Drilling Program.

Yamamoto, Y., Chiyonobu, S., Kanamatsu, T., Ahagon, N., Aoike, K., Kamiya, N., & Kinoshita, M. (2018). Repeated large-scale mass-transport deposits and consequent rapid sedimentation in the western part of the Bay of Bengal, India. *Geological Society, London, Special Publications*. In G. (Vol. 477SP477–12). London: Geological Society. https://doi.org/10.1144/SP477.12

Yamamoto, Y., & Kawakami, S. (2014). Along-Strike Migration of Intermittent Submarine Slope Failures at Subduction Margins: Geological Evidence from the Chikura Group, Central Japan. In *Submarine Mass Movements and Their Consequences*, (pp. 551–560). Cham: Springer. https://doi.org/10.1007/978-3-319-00972-8_49

Yamamoto, Y., Nidaira, M., Ohta, Y., & Ogawa, Y. (2009). Formation of chaotic rock units during primary accretion processes:Examples from the Miura–Boso accretionary complex, central Japan. *Island Arc*, *18*(3), 496–512. https://doi.org/10.1111/j.1440-1738.2009.00676.x

Yamamoto, Y., Ogawa, Y., Uchino, T., Muraoka, S., & Chiba, T. (2007). Large-scalechaotically mixed sedimentary body within the Late Pliocene to Pleistocene Chikura Group, Central Japan. *Island Arc*, *16*(4), 505–507. https://doi.org/10.1111/j.1440-1738.2007.00587.x

Yu, X., Wang, J., Liang, J., Li, S., Zeng, X., & Li, W. (2014). Depositional characteristics and accumulation model of gas hydrates in northern South China Sea. *Marine and Petroleum Geology*, *56*, 74–86. https://doi.org/10.1016/j.marpetgeo.2014.03.011